

Methane emissions from dairies in the Los Angeles Basin

Camille Viatte¹, Thomas Lauvaux², Jacob K. Hedelius¹, Harrison Parker³, Jia Chen^{4,*}, Taylor Jones⁴, Jonathan E. Franklin⁴, Aijun J. Deng², Brian Gaudet², Kristal Verhulst⁵, Riley Duren⁵, Debra Wunch^{1,**}, Coleen Roehl¹, Manvendra K. Dubey³, Steve Wofsy⁴, and Paul O. Wennberg¹

¹ Division of Geological and Planetary Sciences, California Institute of Technology, Pasadena, CA, US

² Department of Meteorology, Pennsylvania State University, University Park, PA, US

³ Earth System Observations, Los Alamos National Laboratory, Los Alamos, NM, US

⁴ School of Engineering and Applied Sciences, Harvard University, Cambridge, MA, US

⁵ Jet Propulsion Laboratory, California Institute of Technology, Pasadena, California, US

* Now at Department of Electrical, Electronic and Computer Engineering, Technical University of Munich, Munich, Germany

** Now at Department of Physics, University of Toronto, Toronto, ON, Canada

16 Abstract

17 We estimate the amount of methane (CH_4) emitted by the largest dairies in the southern
18 California region by combining measurements from four mobile solar-viewing ground-based
19 spectrometers (EM27/SUN), in situ isotopic $^{13/12}\text{CH}_4$ measurements from a CRDS analyzer
20 (Picarro), and a high-resolution atmospheric transport simulation with Weather Research and
21 Forecasting model in Large-Eddy Simulation mode (WRF-LES).

22 The remote sensing spectrometers measure the total column-averaged dry-air mole fractions of
23 CH_4 and CO_2 (X_{CH_4} and X_{CO_2}) in the near infrared region, providing information about total
24 emissions of the dairies at Chino. Differences measured between the four EM27/SUN ranged
25 from 0.2 to 22 ppb (part per billion) and from 0.7 to 3 ppm (part per million) for X_{CH_4} and X_{CO_2} ,
26 respectively. To assess the fluxes of the dairies, these differential measurements are used in
27 conjunction with the local atmospheric dynamics from wind measurements at two local airports
28 and from the WRF-LES simulations at 111 m resolution.

29 Our top-down CH_4 emissions derived using the Fourier Transform Spectrometers (FTS)
30 observations of 1.4 to 4.8 ppt/s are in the low-end of previous top-down estimates, consistent
31 with reductions of the dairy farms and urbanization in the domain. However, the wide range of
32 inferred fluxes points to the challenges posed by heterogeneity of the sources and
33 meteorology. Inverse modeling from WRF-LES is utilized to resolve the spatial distribution of
34 CH_4 emissions in the domain. Both the model and the measurements indicate heterogeneous
35 emissions, with contributions from anthropogenic and biogenic sources at Chino. A Bayesian
36 inversion and a Monte-Carlo approach are used to provide the CH_4 emissions of 2.2 to 3.5 ppt/s
37 at Chino.

38 1) Introduction

39 Atmospheric methane (CH₄) concentration has increased by 150% since the pre-industrial era,
40 contributing to a global average change in radiative forcing of 0.5 W.m⁻² (Foster et al., 2007;
41 Myhre et al., 2013). Methane is naturally emitted by wetlands, but anthropogenic emissions
42 now contribute more than half of its total budget (Ciais et al., 2013), ranking it the second most
43 important anthropogenic greenhouse gas after carbon dioxide (CO₂).

44 The United Nations Framework Convention on Climate Change (UNFCCC,
45 <http://newsroom.unfccc.int/>) aims to reduce CH₄ emissions by reaching global agreements and
46 collective action plans. In the United States (US), the federal government aims to reduce CH₄
47 emissions by at least 17% below 2005 levels by 2020 by targeting numerous key sources such as
48 (in order of importance): agriculture, energy sectors (including oil, natural gas, and coal mines),
49 and landfills (Climate Action Plan, March 2014). Methane emissions are quantified using
50 “bottom-up” and “top down” estimates. The “bottom-up” estimates are based on scaling
51 individual emissions and process level information statistically (such as the number of cows,
52 population density or emission factor) with inherent approximations. “Top-down” estimates,
53 based on atmospheric CH₄ measurements, often differ from these reported inventories both in
54 the total emissions and the partitioning among the different sectors and sources (e.g. Hiller et
55 al., 2014). In the US, the disagreement in CH₄ emissions estimated can reach a factor of two or
56 more (Miller et al., 2013; Kort et al., 2014), and remains controversial regarding the magnitude
57 of emissions from the agricultural sector (Histov et al. 2014). Thus, there is an acknowledged
58 need for more accurate atmospheric measurements to verify the bottom-up estimates (Nisbet
59 and Weiss, 2010). This is especially true in urban regions, such as the Los Angeles basin, where
60 many different CH₄ sources (from farm lands, landfills, and energy sectors) are confined to a
61 relatively small area of ~87000 km² (Wunch et al., 2009; Hsu et al. 2010; Wennberg et al., 2012;
62 Peischl et al., 2013; Guha et al., 2015; Wong et al., 2015). Therefore, improved flux estimations
63 at local scales are needed to resolve discrepancies between bottom-up and top-down
64 approaches and improve apportionment among CH₄ sources.

65 Inventories of CH₄ fluxes suggest that emissions from US agriculture increased by more than
66 10% between 1990 and 2013 (Environmental Protection Agency, EPA, 2015), and by more than
67 20% since between 2000 and 2015 in California (California Air Resources Board, CARB, 2015). In
68 addition, these emissions are projected to increase globally in the future due to increased food
69 production (Tilman and Clark, 2014). Livestock in California have been estimated to account for
70 63% of the total agricultural emissions of greenhouse gases (mainly CH₄ and N₂O); dairy cows
71 represented more than 70% of the total CH₄ emissions from the agricultural sectors in 2013
72 (CARB, 2015). State-wide actions are now underway to reduce CH₄ emissions from dairies (ARB
73 concept paper, 2015). Measurements at the local-scale with high spatial- and temporal-
74 resolution are needed to assess CH₄ fluxes associated with dairy cows and to evaluate the
75 effectiveness of changing practices to mitigate CH₄ emissions from agriculture.

76 Space-based measurements provide the dense and continuous datasets needed to constrain
77 CH₄ emissions through inverse modeling (Streets et al., 2013). Recent studies have used the
78 Greenhouse gases Observing SATellite (GOSAT – footprint of ~10 km diameter) observations to
79 quantify mesoscale natural and anthropogenic CH₄ fluxes in Eurasia (Berchet et al., 2015) and in
80 the US (Turner et al., 2015). However, it is challenging to estimate CH₄ fluxes at smaller spatial
81 scales using satellite measurements due to their large observational footprint (Bréon and Ciais,
82 2010). Nevertheless, recent studies used the SCanning Imaging Absorption spectroMeter for
83 Atmospheric CHartography (SCIAMACHY – footprint of 60 km x 30 km) to assess emissions of a
84 large CH₄ source in the US (Leifer et al., 2013; Kort et al., 2014).

85 Small-scale CH₄ fluxes are often derived from in situ measurements performed at the surface
86 and from towers (Zhao et al., 2009), and/or in situ and remote-sensing measurements aboard
87 aircraft (Karion et al., 2013; Peischl et al., 2013; Lavoie et al., 2015; Gordon et al., 2015). A
88 recent study emphasized the relatively large uncertainties of flux estimates from aircraft
89 measurements using the mass balance approach in an urban area (Cambaliza et al., 2014).

90 Ground-based solar absorption spectrometers are powerful tools that can be used to assess
91 local emissions (McKain et al., 2012). This technique has been used to quantify emissions from
92 regional to urban scales (Wunch et al., 2009; Stremme et al., 2013; Kort et al., 2014;

93 Lindenmaier et al., 2014; Hase et al., 2015; Franco et al., 2015, Wong et al., 2015, Chen et al.,
94 2016; Kille et al., 2017).

95 In this study, we use four mobile ground-based total column spectrometers (called EM27/SUN,
96 Gisi et al., 2012) to estimate CH₄ fluxes from the largest dairy-farming area in the South Coast
97 Air Basin (SoCAB), located in the city of Chino, in San Bernardino County, California. The Chino
98 area was once home to one of the largest concentrations of dairy farms in the United States
99 (US), however rapid land-use change in this area may have caused CH₄ fluxes from the dairy
100 farms change rapidly in both space and time. Chen et al. (2016) used differential column
101 measurements (downwind minus upwind column gradient ΔX_{CH_4} across Chino) recorded on
102 favorable meteorological conditions (e. g. constant wind direction) to verify emissions reported
103 in the literature. In this study, the same column measurement network is employed in
104 conjunction with meteorological data and a high-resolution model to estimate CH₄ emissions at
105 Chino for several different days, including more varying wind conditions. The approach
106 proposed here allows us to describe the spatial distributions of CH₄ emissions within and
107 around the feedlot at very high resolution by using an advanced atmospheric modeling system
108 applicable to any convective meteorological conditions (Gaudet et al., 2017).

109 In section 2 of this paper, the January 2015 field campaign at Chino is described, with details
110 about the mobile column and in situ measurements. In section 3, we describe the new high
111 resolution Weather Research & Forecasting (WRF) model with Large Eddy Simulations (LES)
112 setup. In section 4, results of CH₄ fluxes estimates are examined. Limitations of this approach,
113 as well as suggested future analyses are outlined in section 5.

114 2) Measurements in the Los Angeles Basin dairy farms

115 2.1) Location of the farms: Chino, California

116 Chino (34.02°N, -117.69°W) is located in the eastern part SoCAB, called the Inland Empire, and
117 has historically been a major center for dairy production. With a growing population and
118 expanding housing demand, the agricultural industry has shrunk in this region and grown in the
119 San Joaquin Valley (California Central Valley). The number of dairies decreased from ~400 in the
120 1980's to 95 in 2013 (red area of panels a, b, and c in Figure 1). Nevertheless, in 2013 ~90 % of
121 the southern California dairy cow population (California Agricultural Statistics, 2013) remained
122 within the Chino area of ~6 x 9 km (Figure 1). These feedlots are a major point source of CH₄ in
123 the Los Angeles basin (Peischl et al., 2013).

124 2.2) Mobile column measurements: EM27/SUN

125 Atmospheric column-averaged dry-air mole fractions of CH₄ and CO₂ (denoted X_{CH₄} and X_{CO₂},
126 Wunch et al., 2011) have been measured using four ground-based mobile Fourier Transform
127 Spectrometers (FTS). The mobile instruments were developed by Bruker Optics, are all
128 EM27/SUN models. The four FTS (two owned by Harvard University, denoted Harvard 1 and 2,
129 one owned by Los Alamos National Laboratory, denoted LANL, and one owned by the California
130 Institute of Technology, denoted Caltech, were initially gathered at the California Institute of
131 Technology in Pasadena, California in order to compare them against the existing Total Carbon
132 Column Observing Network (TCCON, Wunch et al., 2011) station and to each other, over several
133 full days of observation. The instruments were then deployed to Chino to develop a
134 methodology to estimate greenhouses gas emissions and improve the uncertainties on flux
135 estimates from this major local source. Descriptions of the capacities and limitations of the
136 mobile EM27/SUN instruments have been published in Chen et al. (2016) and Hedelius et al.
137 (2016). Using Allan analysis, it has been found out that the precision of the differential column
138 measurements ranges between 0.1-0.2 ppb with 10 min averaging time (Chen et al., 2016). For
139 this analysis, we need to ensure that all the data from the EM27/SUN instruments are on the
140 same scale. Here, we reference all instruments to the Harvard2 instrument. Standardized
141 approaches (retrieval consistency, calibrations between the instruments) are needed to

142 monitor small atmospheric gradients using total column measurements from the EM27/SUN.
143 Indeed we ensured all retrievals used the same algorithm, calibrated pressure sensors, and
144 scaled retrievals according to observed, small systematic differences to reduce instrumental
145 biases (Hedelius et al., 2016).

146 These modest resolution (0.5 cm^{-1}) spectrometers are equipped with solar-trackers (Gisi et al.,
147 2011) and measure throughout the day. To retrieve atmospheric total column abundances of
148 CH_4 , CO_2 , and oxygen (O_2) from these Near InfraRed (NIR) solar absorption spectra, we used the
149 GGG software suite, version GGG2014 (Wunch et al., 2015). Column measurements at Chino
150 were obtained on five days: the 15th, 16th, 22nd and 24th of January, and the 13th of August,
151 2015. Of these days, January 15th, 16th, and 24th are sufficiently cloud-free for analysis. These
152 days have different meteorological conditions (i.e. various air temperatures, pressures, wind
153 speeds and directions), improving the representativeness of the flux estimates at Chino.

154 Figure 1 shows measurements made on January 15th, 16th, and 24th. Wind speeds and
155 directions, shown in the bottom panels of Figure 1, are measured at the two local airports
156 inside the domain (the Chino airport indicated on panels d, e, and f and the Ontario airport on
157 panels g, h, and i). Wind measurements from these two airports, located at less than 10 km
158 apart, are made at an altitude of 10 meters above the surface. The exact locations of the four
159 EM27/SUN spectrometers (colored symbols in Figure 1 in the upper panels a, b, and c) were
160 chosen each morning of the field campaign to optimize the chance of measuring upwind and
161 downwind of the plume. On the 15th and 16th of January, the wind speed was low with a
162 maximum of 3 ms^{-1} and highly variable direction all day (Figure 1, panels d, e, g and h),
163 therefore the four EM27/SUN spectrometers were placed at each corner of the source area to
164 ensure that the plume was detected by at least one of the instruments throughout the day. On
165 the contrary, the wind in January 24th had a constant direction from the Northeast and was a
166 relatively strong $8\text{-}10 \text{ ms}^{-1}$ (Figure 1, panels f and i), so the instruments were located such that
167 one spectrometer (Harvard2) was always upwind (blue symbols in Figure 1) and the others are
168 downwind of the plume and at different distances from the sources (black, green, and red
169 symbols in Figure 1).

170 2.3) In situ measurements: Picarro

171 The EM27/SUN column measurements are supplemented by ground-based in situ
172 measurement using a commercial Picarro instruments during January campaign. The Picarro
173 instruments use a Cavity Ringdown Spectroscopy (CRDS) technique that employs a wavelength
174 monitor and attenuation to characterize species abundance.

175 In situ $^{12}\text{CH}_4$, CO_2 , and $^{13}\text{CH}_4$ measurements were performed on January 15th, 16th, and 22nd, and
176 August 13th 2015 at roughly 2m away from the LANL EM27/SUN (Figure 1 a, b, and c) with a
177 Picarro G2132-I instrument (Arata et al., 2016,
178 http://www.picarro.com/products_solutions/isotope_analyzers/). This Picarro, owned by LANL,
179 utilize a 1/4" synflex inlet tube placed approximately 3m above ground level to sample air using
180 a small vacuum pump. Precisions on $^{12}\text{CH}_4$, CO_2 , and $^{13}\text{CH}_4$ measurements are 6 ppb, 2 ppm, and
181 0.6 ‰, respectively.

182 To locate the major CH_4 sources in the dairy farms area, a second Picarro G2401 instrument
183 (http://www.picarro.com/products_solutions/trace_gas_analyzers/) from the Jet Propulsion
184 Laboratory (JPL, Hopkins et al., 2016) was deployed on January 15th, 2015. Precision on CH_4
185 measurements is ~1 ppb.

186 3) Model simulations

187 3.1) Description of WRF-LES model

188 The Weather Research and Forecasting (WRF) model (Skamarock et al., 2008) is an atmospheric
189 dynamics model used for both operational weather forecasting, and scientific research
190 throughout the global community. Two key modules that supplement the baseline WRF system
191 are used here. First, the chemistry module WRF-Chem (Grell et al., 2005) adds the capability of
192 simulating atmospheric chemistry among various suites of gaseous and aerosol species. In this
193 study, CH₄ is modeled as a passive tracer because of its long life time relative to the advection
194 time at local scales. The longest travel time from the emission source region to the instrument
195 locations is less than an hour, which is extremely short compared to the lifetime of CH₄ in the
196 troposphere (~9 years). Therefore, no specific chemistry module is required. The version of
197 WRF-Chem used here (Lauvaux et al., 2012) allowed for the offline coupling between the
198 surface emissions, prescribed prior to the simulation, and their associated atmospheric tracers.
199 Second, we make use of the Large Eddy Simulation (LES) version of WRF (Moeng et al., 2007) on
200 a high-resolution model grid with 111-m horizontal grid spacing. A key feature of the simulation
201 is the explicit representation of the largest turbulent eddies of the Planetary Boundary Layer
202 (PBL) in a realistic manner. The more typical configuration of WRF (and other atmospheric
203 models) is to be run at a somewhat coarser resolution that is incapable of resolving PBL eddies.
204 An advantage in this study is that the effect of the most important PBL eddies to vertical
205 turbulent transport (i.e., the largest eddies) are not parameterized. By having a configuration
206 with the combination of CH₄ tracers and PBL eddies, we can realistically predict the evolution of
207 released material at scales on the order of the PBL depth or smaller. The WRF-LES mode has
208 been evaluated over Indianapolis, IN and compared to the commonly-used mesoscale mode of
209 WRF (Gaudet et al., 2017). The representation of plume structures in the horizontal and in the
210 vertical is significantly improved at short distances (<8km) compared to mesoscale simulations
211 at 1km resolution, while the meteorological performance of WRF-LES remains similar to coarser
212 domains due to the importance of boundary nudging in the nested-domain configuration.
213 Thus, the representation of the CH₄ plumes in this study should be significantly improved with
214 the LES mode configuration of Gaudet et al. (2017).

215 In this real case experiment, the model configuration consists of a series of four one-way
216 nested grids, shown in Figure 2 and described further in the supplementary information section
217 (S1). Each domain contains 201 x 201 mass points in the horizontal, with 59 levels from the
218 surface to 50 hPa, and the horizontal grid spacings are 3 km, 1 km, 333 m, and 111 m. All four
219 domains use the WRF-Chem configuration. The model 3-km, 1-km, and 333-m grids are run in
220 the conventional mesoscale configuration with a PBL parameterization, whereas the 111-m grid
221 physics is LES. The initial conditions for the cases are derived from the National Centers for
222 Environmental Prediction (NCEP) 0.25-degree Global Forecasting System (GFS) analysis fields
223 (i.e., 0-hour forecast) at 6-hour intervals. The simulations are performed from 12:00 to 00:00
224 UTC (= 04:00 to 16:00 LT) only, which corresponds to daylight hours when solar heating of the
225 surface is present and measurements are made.

226 Data assimilation to optimize meteorological fields is performed using Four Dimensional Data
227 Assimilation (FDDA; Deng et al., 2009) for the 3-km and 1-km domains. The assimilation
228 improves the model performance significantly (Rogers et al., 2013; Deng et al., 2017) without
229 interfering with mass conservation and the continuity of the air flow. Surface wind and
230 temperature measurements, including from the Ontario (KONT) and Chino (KCNO) airport
231 stations, and upper-air measurements were assimilated within the coarser grids using the WRF-
232 FDDA system. However, no observations of any kind were assimilated within the 333-m and
233 111-m domains; therefore, the influence of observations can only come into these two domains
234 through the boundary between the 333-m and 1-km grids. Wind measurements at fine scale
235 begin to resolve the turbulent perturbations, which would require an additional pre-filtering.
236 These measurements are used to evaluate the WRF model performances at high resolutions.

237 Based on the terrain elevation in the LES domain (Figure 2), target emissions are located in a
238 triangular-shaped valley with the elevation decreasing gradually towards the South. However,
239 hills nearly surround the valley along the southern perimeter. Meanwhile, the foothills of the
240 San Gabriel Mountains begin just off the 111-m domain boundary to the North. As a result, the
241 wind fields in the valley are strongly modified by local topography, and can be quite different
242 near the surface than at higher levels.

243 3.2) Atmospheric inversion methodology: Bayesian framework and Simulated
244 Annealing error assessment

245 3.2.1 Prior emissions errors: Simulated Annealing

246 The definition of the prior error covariance matrix B is most problematic because little is known
247 about the dairy farms emissions except the presence of cows distributed in lots of small sizes.
248 However, we assume no error correlation as it is known that groups of cows are distributed
249 randomly across our inversion domain. For the definition of the variances in B (i.e. diagonal
250 terms), no reliable error estimate is available because non-agricultural emissions are suspected.
251 The lack of error estimate directly impacts the inverse emissions, and therefore results in the
252 generation of unreliable posterior error estimates. Instead, we develop a Monte-Carlo
253 approach using a Simulated Annealing (SA) technique which will define the range of flux
254 estimates for each grid point according to the observed XCH₄ mole fractions. We test the initial
255 errors in the emissions by creating random draws (i.e. random walk perturbing the emissions
256 iteratively) with an error of about 200% compared to the expected emissions (based on the
257 dairy cows' emissions from CARB 2015). We then generated populations of random solutions
258 and iterated 2000 times with the SA algorithm. Overall, the SA approach allows us to explore
259 the entire space of solutions without any prior constraint. However, we assume here that each
260 pixel is independent, possibly causing biased estimates of CH₄ emissions. To avoid this problem,
261 we only used the range of emission values for each pixel to construct our prior emission errors
262 but discarded the total emissions from the SA. Instead, we performed a Bayesian inversion to
263 produce total emissions for the area, using the diagnosed emissions from the SA as our prior
264 emission errors.

265 3.2.2 Bayesian optimization using WRF-LES

266 Due to the absence of an adjoint model in Large Eddy Simulation mode, the inverse problem is
267 approached with Green's functions, which correspond to the convolution of the Chino dairies
268 emissions and the WRF-LES model response. For the two independent simulations (January 15th
269 and 16th), 16 rectangular areas of 2 x 2 km² (Figure 2) are defined across the feedlots to
270 represent the state vector (x) and therefore the spatial resolution of the inverse emissions,

271 which correspond to the entire dairy farms area of about $8 \times 8 \text{ km}^2$ once combined together.
272 The 16 emitting areas continuously release a known number of CH_4 molecules (prior estimate)
273 during the entire simulations, along with 16 individual tracers representing the 16 areas of the
274 dairies area. The final relationship between each emitting grid-cell and each individual
275 measurement location is the solution to the differential equation representing the sensitivity of
276 each column measurement to the different $2 \times 2 \text{ km}^2$ areas. The WRF-LES results are sampled
277 every 10 minutes at each sampling location to match the exact measurement times and
278 locations of the EM27/SUN instruments.

279 The inversion of the emissions over Chino is performed using a Bayesian analytical framework,
280 described by the following equation:

$$281 \quad x = x_0 + BH^T(HBH^T + R)^{-1}(y - Hx_0) \quad (1)$$

282 with x the inverse emissions, x_0 the prior emissions, B the prior emission error covariance, R
283 the observation error covariance, H the Green's functions, and y the observed column dry air
284 mole fractions. The dimension of the state vector is 16, and we assume constant CH_4 emissions
285 for each individual day. The column observations (here the vector y) correspond to the local
286 enhancements (i.e. the contributions of local sources), the background conditions being
287 subtracted beforehand. Here, we defined the background as the daily minimum for both days,
288 measured by multiple sensors depending on the wind direction and the relative position of the
289 sensor. Figure 3 shows that CH_4 background values vary between 1.830ppm to 1.832ppm, with
290 a minimal value of 1.825ppm on January 16th. We used two distinct daily minimums as our final
291 CH_4 background mixing ratios. The lack of CH_4 inventory for the LA basin and the impact of
292 transport errors on simulated CH_4 mixing ratios are likely to produce larger uncertainties on the
293 background conditions. For these reasons, upwind observations were used to define the
294 background, assuming that spatial gradients across our simulation domain are small compared
295 to atmospheric signals from Chino. The CH_4 observations used here, after subtracting the
296 background value, correspond to local signals of about 10ppb (with a peak at 25ppb), compared
297 to an uncertainty of about 2ppb on the background values. Two maps of 16 emission estimates
298 are produced corresponding to the $2 \times 2 \text{ km}^2$ areas for the two days (January 15th and 16th). A

299 combined inversion provides a third estimate of the emissions using 10-minute average column
300 data from both days. The metric used to select the best solutions is the Mean Absolute Error (or
301 absolute differences) between the simulated and observed column fractions. We store the
302 solutions exhibiting a final mismatch of less than 0.01 ppm to minimize the mismatch between
303 observed and simulated column fractions. The optimal solution and the range of accepted
304 emission scenarios are shown in Figure S2. The space of solutions provide a range of accepted
305 emissions for each $2 \times 2 \text{ km}^2$ area that can be used as a confidence interval in the inversion
306 results. The posterior emissions from the Bayesian inversion are then compared to the
307 confidence interval from the Simulated Annealing to evaluate our final inverse emissions
308 estimates and the posterior uncertainties. The results are presented in Section 4.3.

309 Transport errors in the WRF-LES simulation can impact the accuracy of the inversion and need
310 to be addressed in the optimization. Deng et al. (2017) studied the sensitivity of inverse
311 emissions due to different transport scenarios. To quantify the impact of transport errors on
312 the inverse fluxes, an ensemble approach would be necessary to propagate transport errors in
313 the inverse solution (e.g. Evensen, 1994). Ensemble-based techniques remain computationally
314 expensive, especially for LES simulations. Instead, we aimed at reducing the transport errors
315 using the WRF-FDDA system to limit the errors in wind direction, wind speed, and PBL height.
316 The improvement in model performance is significant, as demonstrated in Deng et al. (2017)
317 reducing by half the wind speed and wind direction random errors, while removing biases in the
318 three variables. Remaining uncertainties are described in the observation error covariance
319 matrix \mathbf{R} by balancing the normalized Chi-squared distance (Lauvaux et al., 2013) varying
320 between 0.5ppb to 3ppb among all the 10-min column measurements.

321 4) Results

322 4.1) Observations of X_{CH_4} and X_{CO_2} in the dairy farms

323 Figure 3 shows the 1-minute average time series of X_{CH_4} (upper panels a, b, and c) and X_{CO_2} (d, e,
324 and f) derived from the four EM27/SUN. For days with slow wind ($\sim 3 \text{ m s}^{-1}$), i.e. on January 15th
325 and 16th (Figure 1, panels d, e, g and h), the maximum gradients observed between the
326 instruments are 17 and 22 ppb (parts per billion), and 2 and 3 ppm (parts per million), for X_{CH_4}

327 and X_{CO_2} , respectively. Assuming that the observed Xgas changes are confined to the PBL,
 328 gradients in this layer are about ten times larger. Gradients observed on January 15th and 16th
 329 are higher than those of X_{CH_4} and X_{CO_2} of 2 ppb and 0.7 ppm observed on a windy day, the 24th.
 330 The X_{CH_4} and X_{CO_2} variabilities captured by the instruments are due to changes in wind speed
 331 and direction, i.e., with high X_{CH_4} signals when the wind blows from the dairies to the
 332 instruments. Thus, the EM27/SUN are clearly able to detect variability of greenhouses gases at
 333 local scales (temporal: less than 5 minutes, and spatial: less than 10 km) indicating that these
 334 mobile column measurements have the potential to provide estimates of local source
 335 emissions.

336 4.2) Estimation of fluxes with EM27/SUN column measurements

337 Total column measurements are directly linked to total emissions (McKain et al., 2012) and are
 338 sensitive to surface fluxes (Keppel-Aleks et al., 2012). To derive the total emissions of trace
 339 gases released in the atmosphere from a source region, the "mass balance" approach is often
 340 used. In its simplest form, the X_{CH_4} fluxes can be written as in Equation 2, but this requires
 341 making assumptions about the homogeneity of the sources and wind shear in the PBL.

$$342 \quad F_{X_{CH_4}} = \Delta_{X_{CH_4}} \frac{V(z)}{m(\theta)} SC_{air}(z) \quad (2)$$

343 where $F_{X_{CH_4}}$ is the flux (molecules/s.m²), $\Delta_{X_{CH_4}}$ is the X_{CH_4} enhancement between the upwind
 344 and the downwind region (ppb), V is the average wind speed (ms⁻¹) from both airports, m is the
 345 distance in meters that air crosses over the dairies calculated as a function of the wind direction
 346 θ , and $SC_{air}(z)$ is the vertical column density of air (molecules/m²). The distances that
 347 airmasses cross over the dairies (m) before reaching a receptor (EM27/SUN) are computed for
 348 each day, each wind direction, and each instrument (see complementary information section
 349 S3).

350 Equation 2 can be reformulated as:

$$351 \quad \Delta_{X_{CH_4}} = \Delta t \cdot \frac{F_{X_{CH_4}}}{SC_{air}(z)} \quad (3)$$

352 where $\Delta t = \frac{m(\theta)}{V(z)}$ is the residence time of air over the dairies (in seconds).

353 A modified version of this mass balance approach has been used by Chen et al. (2016) to verify
354 that the X_{CH_4} gradients measured by the EM27/SUN are comparable to the expected values
355 measured at Chino during the CalNex aircraft campaign (Peischl et al., 2013). In Chen et al., X_{CH_4}
356 enhancements measured between upwind and two of the downwind sites on January 24th (day
357 of constant wind direction, Figure 1 panels f and i) are compared to the expected value derived
358 from Peischl’s emission numbers, which were determined using the bottom-up method and
359 aircraft measurements. They found that the measured X_{CH_4} gradient of ~ 2 ppb, agrees within
360 the low range of the 2010 value. However, this differential approach, using upwind and
361 downwind measurements, reduces the flux estimates to only one day (January 24th), since the
362 wind speed and direction were not constant during the other days of field measurements.

363 In this study, we extend the analysis of the Chino dataset using the mass balance approach on
364 steady-wind day (on January 24th) for all the FTS instruments (i.e three downwind sites), as well
365 as employing the other two days of measurements (January 15th, and 16th) in conjunction the
366 WRF-LES model to derive a flux of X_{CH_4} from the dairy farms. We exclude measurements from
367 January 22nd and August 13th because of the presence of cirrus clouds during those days, which
368 greatly reduce the precision of the column measurements. Our X_{CH_4} signal measured by the FTS
369 can be decomposed as the sum of the background concentration and the enhancements due to
370 the local sources:

$$371 \quad X_{CH_4,measured} = X_{CH_4,background} + \Delta_{X_{CH_4}} \quad (4)$$

372 Gradients of X_{CH_4} ($\Delta_{X_{CH_4}}$) are calculated relative to one instrument for the three days. The X_{CH_4}
373 means (and standard deviations) over the three days of measurements at Chino are 1.824
374 (± 0.003) ppm, 1.833 (± 0.007) ppm, 1.823 (± 0.003) ppm, and 1.835 (± 0.010) ppm for the
375 Caltech, Harvard1, Harvard2, and LANL instruments, respectively. The Harvard2 X_{CH_4} mean and
376 standard deviation are the lowest of all the observations, therefore these measurements are
377 used as ‘background’. This background site is consistent with wind directions for almost all
378 observations, except for small periods of time on January 16th, which highlights the limitation of
379 our method. Gradients of X_{CH_4} ($\Delta_{X_{CH_4}}$) for an instrument i (i.e. Caltech, Harvard1, or LANL) are
380 the differences between each 10-minute average X_{CH_4} measured by i and the simultaneous 10-

381 minute average X_{CH_4} measured by the Harvard2 instrument. Details about the residence time
 382 calculation can be found in the supplementary information section (S3). Time series of
 383 anomalies for individual measurement days are presented in Figure 4.

384 Assuming the background levels X_{CH_4} are similar at all the instrument sites within 10 km
 385 distance and steady state wind fields, equation 3 can be written as:

$$386 \quad (X_{CH_4,i} - X_{CH_4,Harvard2}) \propto (t_i - t_{Harvard2}) \cdot F_{X_{CH_4}} \quad (5)$$

387 Graphical representation of equation 5 is shown in Figure 5 in which $\Delta_{X_{CH_4}}$, the measured
 388 gradients by the four FTS during January 24th, are plotted as a function of Δ_t , so that the slope
 389 corresponds to a flux in ppb/s or ppt/s (parts per trillion). In this figure the slope of the blue
 390 lines (dark and light ones) represents the flux measured at Chino in previous studies (Peischl et
 391 al., 2013). These studies estimating CH_4 fluxes at Chino in 2010 reported a bottom-up value of
 392 28 Gg/yr with a range of top-down measurements from 24 to 74 Gg/yr (Table 1). To compare
 393 these values (in Gg/yr) to the fluxes derived from column average (in ppt/s), we used Equation
 394 6:

$$395 \quad F_{col} = \frac{F \cdot 10^9}{a \cdot Y \cdot SC_{air}(z) \cdot \frac{m_g}{Na}} \cdot 10^{12} \quad (6)$$

396 where F_{col} is the column average flux in ppt/s, F the flux in Gg/yr, a the area of Chino (m^2), Y
 397 the number of seconds in a year, $SC_{air}(z)$ the vertical column density of air ($molecules/m^2$), m_g
 398 the molar mass of CH_4 (g/mol), and Na the Avogadro constant (mol^{-1}).

399 On January 24th, when the wind speed is higher than the other days (Figure 1, panels f, and i),
 400 the residence time over the dairies (Δ_t) is reduced by a factor of 30. The mean Δ_t from the
 401 closest to the furthest instruments to the upwind site are 4 minutes for Caltech (black square,
 402 Figure 5), 13 minutes for Harvard2 (green square, Figure 5), and 16 minutes for LANL (red
 403 square, Figure 5). The X_{CH_4} fluxes estimated using the mean states (mass balance approach) are
 404 4.8, 1.6, and 1.4 ppt/s for the Caltech, LANL, and Harvard2 downwind instruments. For that day,
 405 the high wind speed causes a reduction of the methane plume width across the feedlot, which
 406 may increase uncertainties on the mass-balance approach since the FTS' measurements may
 407 only detect a small portion of the total plume. Overall, the FTS network infers X_{CH_4} emissions at

408 Chino that are in the low-end of previous top-down estimates reported by Peischl et al. (2013),
409 which is consistent with the decrease in cows and farms in the Chino area over several past
410 years.

411 However, the flux estimated using the closest instrument/shortest residence time (i.e. Caltech)
412 exceeds the value from previous studies by almost a factor of two. The other values from LANL
413 and Harvard2, on the other hand, are lower than previous published values. This analysis
414 demonstrates that, even with the steady-state winds day, and the simple geometry, the mass
415 balance still has weaknesses, since it does not properly explain the differences seen among the
416 three downwind sites. The close-in site exhibits the highest apparent emission rate possibly due
417 to the proximity of a large CH₄ source. This exhibits delusive approximations implied by this
418 method (i.e., spatial inhomogeneity of X_{CH₄} sources completely averaged out and conservative
419 transport in the domain) even on the “golden day” of strong steady-state wind pattern.
420 Therefore, when investigating emissions at local scales these assumptions can be dubious and
421 lead to errors in the flux estimates.

422 4.3) Spatial study of the CH₄ fluxes using WRF-LES data

423 Analysis of the spatial sources at Chino is developed in this section using the WRF-LES model
424 and in section 4.4 with in situ Picarro measurements.

425 To map the sources of CH₄ at Chino with the model, we focus on the two days of measurements
426 during which the wind changed direction regularly (i.e. January 15th and 16th, Figure 1 panels d,
427 e, g and h). This provides the model information about the spatial distribution of CH₄ emissions.

428 4.3.1) WRF-LES model evaluation

429 The two WRF-Chem simulations were evaluated for both days (January 15th and 16th) using
430 meteorological observations (Figures 6 and 7). EM27 XCH₄ measurements from January 24th
431 correspond to a constant wind direction and therefore are less suitable for mapping CH₄
432 emissions. The triangulation of sources requires changes in wind direction when using a static
433 network of sensors. Starting with the larger region on the 3-km grid where WMO sondes are
434 available (Figure 6), model verification for both days indicates that wind speed errors averaged

435 over the domain are about 1 ms^{-1} in the free atmosphere and slightly larger in the PBL (less
436 than 2 ms^{-1}). For wind direction, the Mean Absolute Error (MAE) is less than 20 degrees in the
437 free atmosphere and increases approaching the surface, reaching a maximum of about 50
438 degrees there. In the PBL where local enhancements are located, the Mean Error (ME) remains
439 small oscillating between 0 and 10 degrees. At higher resolutions, the comparison between
440 observed and WRF-predicted surface wind speed (Figure 7) indicates that WRF is able to
441 reproduce the overall calm wind conditions for both days at both WMO stations, Chino (KCNO)
442 and Ontario (KONT). However, measurements below 1.5 ms^{-1} are not reported following the
443 WMO standards, which limit the ability to evaluate the model over time. On January 15th at
444 KCNO, consistent with the observations, all domains except the 3-km grid predict no surface
445 wind speeds above 2 ms^{-1} from 16:00 – 19:00 UTC, except for one time from the 111-m LES
446 domain. After this period, the 111-m LES domain successfully reproduces the afternoon peak in
447 wind speed of about 3 ms^{-1} , only slightly smaller than the observed values (3.6 ms^{-1} at Chino
448 and 3.9 ms^{-1} at Ontario airports). However, we should not expect perfect correspondence
449 between the observations and the instantaneous LES output unless a low-pass filter is
450 performed on the LES to average out the turbulence. On January 16th 2015, the model wind
451 speed at KONT remained low throughout the day, in good agreement with the (unreported)
452 measurements, and also with available observations.

453 4.3.2) Dispersion of tracers in LES mode: 15th and 16th January 2015

454 We use the January 15th 2015 case as an example showing the detail in the local winds that can
455 be provided by the high-resolution LES domain. Prior to approximately 19:00 UTC (= 11:00 LT) a
456 brisk easterly flow is present in the valley up to a height of 2 km; however, near the surface, a
457 cold pool up to several hundred meters thick developed with only a very weak easterly motion.
458 A simulated tracer released from a location near the east edge of the Chino area stays confined
459 to the cold pool for this period (Figure 8, upper row). Solar heating causes the cold pool to
460 break down quite rapidly after 19:00 UTC, causing the low-level wind speed to become more
461 uniform with height (around 3 ms^{-1} from the east), and allowing the tracer to mix up to a height
462 of about 1 km (Figure 8, middle row). Beginning around 22:00 UTC (= 14:00 LT) however, a
463 pulse of easterly flow scours out the valley from the east, while a surge of cooler westerly flow

464 approaches at low levels from the west, undercutting the easterly flow. By 00:00 UTC (=16:00
465 LT) the tracer seems to be concentrated in the cooler air just beneath the boundary of the two
466 opposing air streams (Figure 8, lower row).

467 The tracer released (right columns in Figure 8) from an emitting $2 \times 2 \text{ km}^2$ pixel shows complex
468 vertical structures and two different regimes over the day. At 18:00 UTC, the tracer is
469 concentrated near the surface, except toward the West with a maximum at 600 m high. At
470 21:00 UTC, the tracer is well-mixed in the vertical across the entire PBL, from 0 to about $\sim 1 \text{ km}$,
471 corresponding to convective conditions of daytime. At 00:00 UTC, the stability increased again,
472 generating a low vertical plume extent with complex structures and large vertical gradients
473 along the transect. Several updrafts and downdrafts are visible at 18:00 and 00:00 UTC,
474 indicated by the shift in wind vectors and the distribution of the tracer in the vertical (Figure 8).
475 These spatial structures are unique to the LES simulation, as the PBL scheme of the mesoscale
476 model does not reproduce turbulent eddies within the PBL.

477 In the horizontal, convective rolls and large tracer gradients are present, with visible fine-scale
478 spatial structures driven by the topography (i.e. hills in the South of the domain) and turbulent
479 eddies. Figure 9 (left panel) illustrates the spatial distribution of the mean horizontal wind at
480 the surface over the 111-m simulation domain at 18:00 UTC, just prior to the scouring out of
481 the cold pool near a large Chino feedlot. It can be seen that the near-surface air that fills the
482 triangular valley in the greater Chino area is nearly stagnant, while much stronger winds appear
483 on the ridges to the south. There are some banded structures showing increased wind speed
484 near KONT to the north of the main pool of stagnant air. Figure 9 (right panel) illustrates the
485 wind pattern for the 18:00 UTC January 16th case. The same general patterns can be seen, with
486 the main apparent differences being reduced wind speed along the southern high ridges, and
487 more stagnant air in the vicinity of KONT along with elevated wind speed bands near KCNO.
488 These results emphasize how variable the wind field structures can be from point-to-point in
489 the valley.

490 4.3.3) Bayesian inversion and error assessment

491 We present the inverse emissions from the Bayesian analytical framework with probability
492 distribution functions from the Simulated Annealing in Figure 10. The Bayesian analytical
493 solution was computed for both days, assuming a flat prior emission rate of $2150 \text{ mol/km}^2/\text{hour}$
494 corresponding to a uniform distribution of 115000 dairy cows over 64 km^2 emitting methane at
495 a constant rate of 150 kg of CH_4 per year (CARB 2015), plus 18 kg annually per cow from dry
496 manure management assumed to be on-site (Peischl et al., 2013). The colored contours in
497 Figure 10 represent the probability density (or confidence level) defined by the Simulated
498 Annealing (SA) analysis for the two days of the campaign. The Bayesian averages are
499 moderately correlated with high confidence solutions from the SA. However, the highest value
500 (pixel 2) coincides with high confidence for large emission values (>50% probability of
501 emissions at $8,000 \text{ mol/km}^2/\text{hour}$ or higher in pixels 2 or 3) which confirms that large flux signals
502 are fairly well constrained in the inverse solution. Other pixels (i.e. 6 to 11) show a wide range
503 of high confidence values meaning that the inverse solution is more uncertain at these
504 locations, with few pixels being completely unconstrained (i.e. with low probabilities from the
505 SA analysis such as pixels 15 and 16). This would possibly suggest that only the largest emissions
506 could be attributed with sufficient confidence using these tools.

507 The spatial distribution of the emissions is shown in Figure 13, which directly corresponds to
508 the pixel emissions presented in Figure 10. The largest sources are located in the southern part
509 of the dairy farms area, and in the northeastern corner of the domain. Additional interpretation
510 of these results is presented in the following section. The combination of the results from two
511 dates (January 15th and 16th) is necessary in order to identify the whole southern edge of the
512 feedlots as a large source. Sensitivity results are presented in the discussion and in the
513 supplementary information section (S4 and S5). The triangulation of sources performed by the
514 inversion produced consistent results using different configurations of EM27 sensors for each
515 day. Inversion results cover the entire domain with all wind directions being observed over the
516 two days (cf. Figure 1, panels d, e, g, and h). Additional sensitivity tests were performed to
517 evaluate the impact of instrument errors, introducing a systematic error of 5 ppb in X_{CH_4}
518 measured by one of the EM27/SUN. The posterior emissions increased by 3-4 Gg/year for a

519 +5ppb bias almost independent of the location of the biased instrument. This represents ~10%
520 of the total emission at Chino.

521 4.4) Spatial study of the CH₄ emissions at Chino using Picarro measurements

522 During the field campaign in January 2015, in situ measurements of CH₄, CO₂, as well as δ¹³C are
523 collected simultaneously with a Picarro instrument at the same site as the LANL EM27/SUN.
524 Fossil-related CH₄ sources, such as power plants, traffic, and natural gas, emit CH₄ with an
525 isotopic depletion δ¹³C ranging from -30 to -45 ‰, whereas biogenic methane sources, such as
526 those from enteric fermentation and wet and dry manure management in dairies and feedlots
527 emit in the range of -65 to -45 ‰ (Townsend-Small et al., 2012). During the January 2015
528 campaign, the δ¹³C at Chino ranged from -35 to -50 ‰, indicating a mixture of fossil and
529 biogenic sources respectively. Most of the air sampled included a mixture of both sources.
530 However, the measurements with the highest CH₄ concentrations had lowest δ¹³C signatures,
531 suggesting that the major CH₄ enhancements measured by the Picarro instrument can be
532 attributed to the dairy farms and not the surrounding urban sources.

533 On January 16th and 22nd, the Picarro and the LANL EM27/SUN were installed at the southwest
534 side of the largest dairies in Chino (red pin, Figure 1b), near a wet lagoon that is used for
535 manure management (< 150 m away). For these days, the Picarro measured enhancements of
536 CH₄ up to 20 ppm above background concentrations, demonstrating that the lagoon is a large
537 source of CH₄ emissions in the Chino area. The location of the lagoon was identified and verified
538 by satellite imagery, visual inspection, and also with measurements from the second Picarro
539 instrument deployed in the field on January 15th, 2015. With this instrument, CH₄ spikes up to
540 23 ppm were observed near the wet manure lagoon. The measurements from both Picarras
541 and the LANL EM27/SUN instrument near the lagoon suggested that this is a significant local
542 source of CH₄ emissions in the Chino area.

543 As opposed to column measurements, Picarro measurements are very sensitive to the dilution
544 effect of gases in the PBL. With a low boundary layer, atmospheric constituents are
545 concentrated near the surface, and the atmospheric signal detected by the in situ surface
546 measurements is enhanced relative to the daytime, when the PBL is fully developed. For this

547 reason, additional Picarro measurements were made at night on August 13th 2015, when the
548 PBL height is minimal. Between 04:00 to 07:00 (LT), we performed Picarro measurements at
549 different locations in Chino, to map the different sources of CH₄ and verify that the large
550 sources observed in January, such as the lagoon, are still emitting in summer. Figure 11 shows
551 the scatter plot of one minute-average anomalies of CH₄ (Δ_{CH_4}) versus CO₂ (Δ_{CO_2}), colored by
552 the $\delta^{13}C$ values, measured by the Picarro on the night of August 13th 2015. During that night,
553 the isotopic range of $\delta^{13}C$ in sampled methane range from -45 ‰ to -65 ‰. These low $\delta^{13}C$
554 values are consistent with the expectation that the sources of CH₄ in the Chino area are
555 dominated by biogenic emissions from dairy cows. In the feedlots (side triangles, Figure 11),
556 Δ_{CH_4} and Δ_{CO_2} are well correlated ($r^2 = 0.90$), because cows emit both gases (Kinsman et al.,
557 1995). The observed $\Delta_{CH_4}/\Delta_{CO_2}$ emission ratio, 48 ± 1.5 ppb/ppm, is in good agreement with a
558 previous study measuring this ratio from cow's breath (Lassen et al., 2012). Measurements
559 obtained at less than one meter away from cows (circles, Figure 11), had the lowest the $\delta^{13}C$
560 observed, ~ -65 ‰, and these points scale well with the linear correlation observed during the
561 survey. This confirms that the emission ratio derived surveying the feedlots is representative of
562 biogenic emissions related to enteric fermentation. Measurements obtained next to the lagoon
563 (diamond marks, Figure 11), the ¹²CH₄ concentrations enhanced by up to 40 ppm above
564 background levels observed that night, while the relative enhancement of CO₂ was much
565 smaller. This extremely large CH₄ enhancement relative to CO₂ indicates a signature of CH₄
566 emissions from wet manure management (lagoon), confirming that there is significant
567 heterogeneity in the CH₄ sources within the Chino dairy area.

568 5) Discussion

569 The fluxes derived by the FTS observations and the WRF-LES inversions, as well as previous
570 reported values are summarized in Table 1.

571 The top-down CH₄ estimate using FTS observations in Chino provide a range of fluxes from 1.4
572 to 4.8 ppt/s during January 2015 (Table 1), which are on the lower-end of previously published
573 estimates. These values of CH₄ flux estimates for January 2015 based on the FTS measurements
574 are consistent with the decrease in cows in Chino over the past several years as urbanization
575 spreads across the region. The mass-balance approach uses a simple characterization of the
576 background X_{CH₄} that can be applied to any deployment of EM27 sensors. As described in S3,
577 emissions are estimated using the average residence time between the sensor locations based
578 on meteorological measurements. The wind direction has not been considered here to perform
579 a site selection and define background X_{CH₄} mole fractions. Therefore, the range of emissions
580 from our analysis may be larger possibly due to variations in the observed enhancements when
581 the mean wind direction changes frequently over the day. The approach presented here could
582 be improved by collecting wind direction measurements co-located to EM27 sensors to help
583 define the boundary conditions (as described in Lauvaux et al., 2016).

584 Considering the decrease of dairy cows number by ~20% from 2010 to 2015, and using the
585 emission factor of 168 kg/yr per head (CARB 2015 inventory: enteric fermentation + dry manure
586 management), the CH₄ flux associated with dairy cows at Chino decreased from 2.0 to 1.7 ppt/s,
587 which agrees well with our low flux estimates derived from FTS observations. However, fluxes
588 derived using the simple mass balance approach differs from each other, exhibiting the
589 limitations of this method, even on a “golden day” (steady-state wind day on January 24th). The
590 WRF-LES inversions (Figures 10 and 12) and mobile in situ measurements with the Picarro
591 instrument (Figure 11) indicate that the CH₄ sources are not homogeneous within this local
592 area. In addition, wind measurements from the two local airports typically disagree regarding
593 the direction and speed (Figure 1, panels d, e, f, g, h, and i), and the WRF-LES tracer results
594 indicate non-homogeneous advection of tracers (Figure 8, right panels).

595 Figure 12 shows the map of the *a posteriori* X_{CH_4} fluxes (mean of January 15th and 16th runs)
596 from the WRF-LES simulations, superimposed on a Google earth map, with the location of dairy
597 farms represented by the red areas. The domain is decomposed into 16 boxes (Section 3.2), in
598 which the colors correspond to the *a posteriori* emissions derived from the WRF-LES inversions.
599 Red (blue) colors of a box mean more (less) CH_4 emissions compared to the *a priori* emissions,
600 which corresponds to the dairy cow emissions contained in the CARB 2015 inventory (emission
601 factor multiplied by the number of cows). Results of the inversion exhibit more CH_4 emissions
602 at the South and the Northeast parts of the domain, and emissions corresponding to dairy cows
603 in the center of the area.

604 The higher CH_4 emissions from the southwestern part of the domain can be attributed to the
605 wet manure lagoon (yellow pin, Figure 12) in January 2015. During the night of August 13th
606 2015, Picarro measurements confirmed that the lagoon was still wet and emitted a
607 considerable amount of CH_4 relative to CO_2 (Figure 12). The second mobile Picarro instrument
608 from JPL was deployed on January 15th 2015 and measured CH_4 spikes up to 23 ppm near the
609 wet manure lagoon. The WRF-LES model also suggests higher methane fluxes in these regions
610 (red boxes, Figure 12). The CARB 2015 inventory estimates that manure management practices
611 under wet (e.g. lagoon) conditions emit more CH_4 than the dairy cows themselves: 187 kg CH_4
612 $\text{cow}^{-1} \text{yr}^{-1}$ from wet manure management, 18 kg $\text{CH}_4 \text{cow}^{-1} \text{yr}^{-1}$ from dry management practices,
613 and 150 kg $\text{CH}_4 \text{cow}^{-1} \text{yr}^{-1}$ from enteric fermentation in the stomachs of dairy cows. Therefore,
614 we expect measurements in which the lagoon emissions were detected by our instruments will
615 lead to higher methane fluxes in the local region, compared to measurements detecting
616 emissions from enteric fermentation in cows alone. Bottom-up emission inventory of CH_4 is 2
617 times higher when considering wet lagoons (Wennberg et al., 2012) instead of dry management
618 practices (Peischl et al., 2013) at Chino (Table1). The location and extent of wet lagoons in the
619 Chino region is not expected to be constant with time and could be altered due to changing
620 land use and future development in the area. Bottom-up estimates of CH_4 emissions from
621 dairies in the Chino region could be further improved if the extent and location of wet manure
622 lagoons were well-known.

623 The WRF-LES model also suggests higher methane fluxes in the Southeast (red boxes, Figure
624 13). No dairy farms are located in these areas, but an inter-state pipeline is located nearby, thus
625 these CH₄ enhancements could be attributed to natural gas. The ¹³CH₄ Picarro measurements
626 indicate the Chino area is influenced by both fossil- and biogenic- related methane sources. A
627 recent study has suggested the presence of considerable fugitive emissions of methane at
628 Chino (<http://www.edf.org/climate/methanemaps/city-snapshots/los-angeles-area>), probably
629 due to the advanced age of the pipelines. Natural gas leaks in the Chino area were not
630 specifically targeted during the time of this field campaign and cannot be confirmed using
631 available data. This possibility should thus be confirmed by future studies.

632 In addition to possible fugitive emissions at Chino, the inversion also predicts higher CH₄ flux in
633 the Northeastern region of the study domain, which is in the vicinity of a power plant that
634 reportedly emits a CH₄ flux roughly equivalent of one cow per year (only including enteric
635 fermentation) (http://www.arb.ca.gov/cc/reporting/ghg-rep/reported_data/ghg-reports.htm).
636 Further analysis and measurements of fossil methane sources in the Chino area would help
637 verify potential contributions from fossil methane sources, including power plants and/or
638 fugitive natural gas pipeline emissions.

639 Overall, FTS and in situ Picarro measurements, as well as WRF-LES inversions, all demonstrate
640 that the CH₄ sources at Chino are heterogeneous, with a mixture of emissions from enteric
641 fermentation, wet and dry manure management practices, and possible additional fossil
642 methane emissions (from natural gas pipeline and power plants). The detection of CH₄
643 emissions in the Chino region and discrepancies between top-down estimates could be further
644 improved with more FTS observations and concurrent in situ methane isotopes measurements
645 combined with high-resolution WRF-LES inversions. This would improve the spatial detection of
646 the CH₄ emissions at Chino, in order to ameliorate the inventories among the individual sources
647 in this local area.

648 6) Summary and conclusions

649 In January 2015, four mobile low-resolution FTS (EM27/SUN) were deployed in a ~6 x 9 km area
650 in Chino (California), to assess CH₄ emissions related to dairy cows in the SoCAB farms. The
651 network of column measurements captured large spatial and temporal gradients of
652 greenhouses gases emitted from this small-scale area. Temporal variabilities of X_{CH₄} and X_{CO₂}
653 can reach up to 20 ppb and 2 ppm, respectively, within less than a 10-minute interval with
654 respect to wind direction changes. This study demonstrate that these mobile FTS are therefore
655 capable of detecting local greenhouses gas signals and these measurements can be used to
656 improve the verification of X_{CO₂} and X_{CH₄} emissions at local scales.

657 Top-down estimates of CH₄ fluxes using the 2015 FTS observations in conjunction with wind
658 measurements are 1.4-4.8 ppt/s, which are in the low-end of the 2010 estimates (Peischl et al.,
659 2013), consistent with the decrease in cows in the Chino area. During this campaign, FTS
660 measurements were collected in close proximity to the sources (less than a few km) in order to
661 capture large signals from the local area. The main advantage of this type of deployment
662 strategy is to better constrain the emissions, while avoiding vertical mixing issues in the model
663 with the use of column measurements in the inversion (Wunch et al., 2011). Therefore, the
664 model transport errors, which often limit the capacity of the model flux estimates, are
665 considerably reduced. However, the close proximity of the measurements to the sources makes
666 the assumptions about homogeneity of the sources and wind patterns questionable.

667 The FTS and the Picarro measurements detected various CH₄ signatures over Chino, with
668 extreme CH₄ enhancements measured nearby a wet lagoon (Picarro and FTS measurements
669 enhanced by 40 ppm CH₄ and 60 ppb X_{CH₄}, respectively) and possible fugitive fossil-related CH₄
670 emissions in the area (indicated by higher δ¹³C values than expected from biogenic emissions
671 alone).

672 Wind speed and direction measurements derived from the two local airports (less than 10 km
673 apart), as well as the WRF meteorological simulations at different FTS sites, differ greatly with
674 each other, suggesting that an assumption of steady horizontal wind can be improved upon in
675 the use of the mass balance approach in our study.

676 This study demonstrates the value of using mobile column measurements for detection of local
677 CH₄ enhancements and the estimation of CH₄ emissions when these measurements are
678 combined with modeling. High-resolution (111 m) WRF-LES simulations were performed on two
679 dates, constrained by four column measurements each day, to map the heterogeneous CH₄
680 sources at Chino. The optimized emissions (i.e. average a posteriori flux) over the domain are
681 1.3 ppt/s when only considering the boxes in the center of the domain, and 2.6 ppt/s when all
682 the boxes are averaged. A major emitter (a wet manure lagoon) was identified by the inversion
683 results, and is supported by in-situ ¹³CH₄ measurements collected during the campaign. The CH₄
684 flux estimates are within the range of the top-down mass balance emissions derived with the
685 four FTS and estimates reported by Peischl et al. 2013 (i.e., 2.1 to 6.5 ppt/s), showing that
686 column measurements combined with high resolution modeling can detect and be used to
687 estimate CH₄ emissions.

688 The instrumental synergy (mobile in situ and column observations) coupled with a
689 comprehensive high-resolution model simulations allow estimation of local CH₄ fluxes, and can
690 be useful for improving emission inventories, especially in a complex megacity area, where the
691 different sources are often located within small areas.

692 This study highlights the complexity of estimating emissions at local scale when sources and
693 wind can exhibit heterogeneous patterns. Long term column observations and/or aircraft eddy
694 covariance measurements could improve estimations.

695 Acknowledgements:

696 The authors thank NASA and the W. M. Keck Institute for Space Studies for financial support.
697 MKD acknowledges NASA CMS support of the EM27/SUN deployment and LANL- LDRD
698 20110081DR for acquisition of the instrument. J. Chen, T. Jones, J. E. Franklin, and S. C. Wofsy
699 gratefully acknowledge funding provided by the National Science Foundation through MRI
700 Award 1337512. A portion of this research was carried out at the Jet Propulsion Laboratory,
701 California Institute of Technology, under contract with the National Aeronautics and Space
702 Administration. January Campaign participants are Camille Viatte, Jacob Hedelius, Harrison
703 Parker, Jia Chen, Johnathan Franklin, Taylor Jones, Riley Duren, and Kristal Verhulst.

704
705
706
707
708
709
710
711
712
713
714
715
716
717
718
719
720
721
722
723
724
725
726
727
728

References:

Air Resources Board (ARB): concept paper, full report, May 7th 2015, available at: http://www.arb.ca.gov/cc/shortlived/concept_paper.pdf, 2015.

Arata, C., Rahn, T., and Dubey, M. K.: Methane Isotope Instrument Validation and Source Identification at Four Corners, New Mexico, United States, *J. Phys. Chem. A*, doi: 10.1021/acs.jpca.5b12737, 2016.

Berchet, A., Pison, I., Chevallier, F., Paris, J.-D., Bousquet, P., Bonne, J.-L., Arshinov, M. Y., Belan, B. D., Cressot, C., Davydov, D. K., Dlugokencky, E. J., Fofonov, A. V., Galanin, A., Lavrič, J., Machida, T., Parker, R., Sasakawa, M., Spahni, R., Stocker, B. D., and Winderlich, J.: Natural and anthropogenic methane fluxes in Eurasia: a mesoscale quantification by generalized atmospheric inversion, *Biogeosciences*, 12, 5393-5414, doi:10.5194/bg-12-5393-2015, 2015.

Breon, F. M. and Ciais, P.: Spaceborne remote sensing of greenhouse gas concentrations, *Comptes Rendus Geoscience*, 342, 412–424, doi: 10.1016/j.crte.2009.09.012, 2010.

California Agricultural Statistics, United States Department of Agriculture, National Agricultural Statistics Service, Pacific Regional, Field Office California, full report, available at: http://www.nass.usda.gov/Statistics_by_State/California/Publications/California_Ag_Statistics/CALivestockandDairy.pdf, 2013.

California Air Resources Board (CARB): California Greenhouse Gas Emission Inventory - 2015 Edition, available from: <http://www.arb.ca.gov/cc/inventory/data/data.htm>, 2015.

Cambaliza, M. O. L., Shepson, P. B., Caulton, D. R., Stirm, B., Samarov, D., Gurney, K. R., Turnbull, J., Davis, K. J., Possolo, A., Karion, A., Sweeney, C., Moser, B., Hendricks, A., Lauvaux, T., Mays, K., Whetstone, J., Huang, J., Razlivanov, I., Miles, N. L., and Richardson, S. J.: Assessment of uncertainties of an aircraft-based mass balance approach for quantifying urban greenhouse gas emissions, *Atmos. Chem. Phys.*, 14, 9029–9050, doi:10.5194/acp-14-9029-2014, 2014.

729 Chen, J., Viatte, C., Hedelius, J. K., Jones, T., Franklin, J. E., Parker, H., Gottlieb, E. W., Wennberg,
730 P. O., Dubey, M. K., and Wofsy, S. C.: Differential Column Measurements Using Compact Solar-
731 Tracking Spectrometers, *Atmos. Chem. Phys.*, 16, 8479–8498, doi:10.5194/acp-16-8479-2016,
732 2016.

733 Ciais, P., Sabine, C., Bala, G., Bopp, L., Brovkin, V., Canadell, J., Chhabra A., DeFries, R., Galloway,
734 J., Heimann, M., Jones, C., Le Quéré, C., Myneni, R.B., Piao, S., and Thornton, P.: Carbon and
735 Other Biogeochemical Cycles. In: *Climate Change 2013: The Physical Science Basis. Contribution of Working Group I to the Fifth Assessment Report of the Intergovernmental Panel on Climate Change* [Stocker, T.F., Qin, D., Plattner, G.-K., Tignor, M., Allen, S.K., Boschung, J., Nauels, A., Xia, Y., Bex, V. and Midgley, P.M. (eds.)]. Cambridge University Press, Cambridge,
736 United Kingdom and New York, NY, USA, 2013.

740 Deng, A., Stauffer, D., Gaudet, B., Dudhia, J., Hacker, J., Bruyere, C., Wu, W., Vandenberghe, F.,
741 Liu, Y., and Bourgeois, A.: Update on WRF-ARW end-to-end multi-scale FDDA system. 10th
742 Annual WRF Users' Workshop, Boulder, CO, 23 Jun 2009.

743 Deng, A., Lauvaux, T., Davis, K.J., Gaudet, B. J., Miles, N. L., Richardson, S. J., Wu, K., Sarmiento,
744 D. P., Hardesty, R. M., Bonin, T. A., Brewer, W. A., and Gurney, K. R.: Toward reduced transport
745 errors in a high resolution urban CO₂ inversion system, accepted, *Elementa*.

746 Environmental Protection Agency (EPA): Sources of Greenhouses Gases Emissions: addresses
747 anthropogenic emissions from agricultural activities (not including fuel combustion and sewage
748 emissions, which are addressed in the Energy and Waste chapters), full report, available from:
749 [http://www.epa.gov/climatechange/Downloads/ghgemissions/US-GHG-Inventory-2015-](http://www.epa.gov/climatechange/Downloads/ghgemissions/US-GHG-Inventory-2015-Chapter-5-Agriculture.pdf)
750 [Chapter-5-Agriculture.pdf](http://www.epa.gov/climatechange/Downloads/ghgemissions/US-GHG-Inventory-2015-Chapter-5-Agriculture.pdf), 2015.

751 Evensen, G.: Sequential data assimilation with a nonlinear quasi-geostrophic model using
752 Monte Carlo methods to forecast error statistics, *J. Geophys. Res.*, 99(C5), 10143–10162,
753 doi:10.1029/94JC00572, 1994.

754 Forster, P., Ramaswamy, V., Artaxo, P., Bernsten, T., Betts, R., Fahey, D.W., Haywood, J., Lean,
755 J., Lowe, D.C., Myhre, G., Nganga, J., Prinn, R., Raga, G. M. S., Van Dorland, R.: Changes in
756 Atmospheric Constituents and in Radiative Forcing. In: S. Solomon et al. (Editors), *Climate*
757 *Change 2007: The Physical Science Basis. Contribution of Working Group I to the Fourth*

758 Assessment Report of the Intergovernmental Panel on Climate Change. Cambridge University
759 Press, Cambridge, U.K, doi:10.1017/CBO9781107415324, 2007.

760 Franco, B., Hendrick, F., Van Roozendaal, M., Müller, J.-F., Stavrou, T., Marais, E. A., Bovy, B.,
761 Bader, W., Fayt, C., Hermans, C., Lejeune, B., Pinardi, G., Servais, C., and Mahieu, E.: Retrievals
762 of formaldehyde from ground-based FTIR and MAX-DOAS observations at the Jungfraujoch
763 station and comparisons with GEOS-Chem and IMAGES model simulations, *Atmos. Meas. Tech.*,
764 8, 1733-1756, doi:10.5194/amt-8-1733-2015, 2015.

765 Gaudet, B. J., Lauvaux, T., Deng, A., Davis, K. J.: Exploration of the impact of nearby sources on
766 urban atmospheric inversions using large eddy simulation, *Elementa*, in review, 2017.

767 Gisi, M., Hase, F., Dohe, S., and Blumenstock, T.: Camtracker: a new camera controlled
768 high precision solar tracker system for FTIR-spectrometers, *Atmos. Meas. Tech.*, 4, 47–54,
769 doi:10.5194/amt-4-47-2011, 2011.

770 Gisi, M., Hase, F., Dohe, S., Blumenstock, T., Simon, A., and Keens, A.: XCO₂-measurements with
771 a tabletop FTS using solar absorption spectroscopy, *Atmos. Meas. Tech.*, 5, 2969–2980,
772 doi:10.5194/amt-5-2969-2012, 2012.

773 Gordon, M., Li, S.-M., Staebler, R., Darlington, A., Hayden, K., O'Brien, J., and Wolde, M.:
774 Determining air pollutant emission rates based on mass balance using airborne measurement
775 data over the Alberta oil sands operations, *Atmos. Meas. Tech.*, 8, 3745-3765, doi:10.5194/amt-
776 8-3745-2015, 2015.

777 Grell, G.A., Peckham, S.E., Schmitz, R., McKeen, S.A., Frost, G., Skamarock, W.C., and Eder, B.:
778 Fully coupled online chemistry within the WRF model, *Atmos. Environ.*, 39, 6957–6975, 2005.

779 Guha, A., Gentner, D. R., Weber, R. J., Provencal, R., and Goldstein, A. H.: Source apportionment
780 of methane and nitrous oxide in California's San Joaquin Valley at CalNex 2010 via positive
781 matrix factorization, *Atmos. Chem. Phys. Discuss.*, 15, 6077-6124, doi:10.5194/acpd-15-6077-
782 2015, 2015.

783 Hase, F., Frey, M., Blumenstock, T., Groß, J., Kiel, M., Kohlhepp, R., Mengistu Tsidu, G.,
784 Schäfer, K., Sha, M. K., and Orphal, J.: Use of portable FTIR spectrometers for detecting
785 greenhouse gas emissions of the megacity Berlin – Part 2: Observed time series of X_{CO_2} and
786 X_{CH_4} , *Atmos. Meas. Tech. Discuss.*, 8, 2767-2791, doi:10.5194/amtd-8-2767-2015, 2015.

787 Hedelius, J. K., Viatte, C., Wunch, D., Roehl, C. M., Toon, G. C., Chen, J., Jones, T., Wofsy, S. C.,
788 Franklin, J. E., Parker, H., Dubey, M. K., and Wennberg, P. O.: Assessment of errors and biases in
789 retrievals of X_{CO_2} , X_{CH_4} , X_{CO} , and X_{N_2O} from a 0.5 cm^{-1} resolution solar-viewing spectrometer,
790 *Atmos. Meas. Tech.*, 9, 3527-3546, doi:10.5194/amt-9-3527-2016, 2016.

791 Hiller, R. V., Neininger, B., Brunner, D., Gerbig, C., Bretscher, D., Künzle, T., Buchmann, N., and
792 Eugster, W.: Aircraft-based CH_4 flux estimates for validation of emissions from an agriculturally
793 dominated area in Switzerland, *J. Geophys. Res. Atmos.*, 119, doi:10.1002/2013JD020918, 2014.

794 Histov, A. N., Johnson, K. A., and Kebreab, E.: Livestock methane emissions in the United States,
795 *P. Natl. Acad. Sci.*, 111 (14), E1320, doi: 10.1073/pnas.1401046111, 2014.

796 Hopkins, F. M., Kort, E. A., Bush, S. E., Ehleringer, J. R., Lai, C.-T., Blake, D. R., and Randerson, J.
797 T.: Spatial patterns and source attribution of urban methane in the Los Angeles Basin, *J.*
798 *Geophys. Res. Atmos.*, 121, 2490–2507, doi:10.1002/2015JD024429, 2016.

799 Hsu, Y.-K., VanCuren, T., Park, S., Jakober, C., Herner, J., FitzGibbon, M., Blake, D. R., and
800 Parrish, D. D.: Methane emissions inventory verification in southern California, *Atmos. Environ.*,
801 44, 1–7, doi:10.1016/j.atmosenv.2009.10.002, 2010.

802 Intergovernmental Panel on Climate Change (IPCC): Climate Change 2013: the physical science
803 basis. Contribution of working group I to the fifth Assessment report of the Intergovernmental
804 Panel On Climate Change [Stocker, T.F., Qin, D., Plattner, G.-K., Tignor, M., Allen, S.K., Boschung,
805 J., Nauels, A., Xia, Y., Bex, V. and Midgley, P.M. (eds.)]. Cambridge University Press, Cambridge,
806 United Kingdom and New York, NY, USA, 1535pp, 2013.

807 Karion, A., Sweeney, C., Pétron, G., Frost, G., Michael Hardesty, R., Kofler, J., Miller, B. R.,
808 Newberger, T., Wolter, S., Banta, R., Brewer, A., Dlugokencky, E., Lang, P., Montzka, S. A.,
809 Schnell, R., Tans, P., Trainer, M., Zamora, R., and Conley, S.: Methane emissions estimate from

810 airborne measurements over a western United States natural gas field, *Geophys. Res. Lett.*, 40,
811 4393–4397, doi: 10.1002/grl.50811, 2013.

812 Keppel-Aleks, G., Wennberg, P.O., Washenfelder, R.A., Wunch, D., Schneider, T., Toon, G.C.,
813 Andres, R.J., Blavier, J.-F., Connor, B., Davis, K.J., Desai, A.R., Messerschmidt, J., Notholt, J.,
814 Roehl, C.M., Sherlock, V., Stephens, B.B., Vay, S.A., and Wofsy, S.C.: The imprint of surface
815 fluxes and transport on variations in total column carbon dioxide, *Biogeosciences*, 9, 875–891,
816 doi:10.5194/bg-9-875-2012, 2012.

817 Kille, N., Baidar, S., Handley, P., Ortega, I., Sinreich, R., Cooper, O. R., Hase, F., Hannigan, J. W.,
818 Pfister, G., and Volkamer, R.: The CU mobile Solar Occultation Flux instrument: structure
819 functions and emission rates of NH₃, NO₂ and C₂H₆, *Atmos. Meas. Tech.*, 10, 373-392,
820 doi:10.5194/amt-10-373-2017, 2017.

821 Kinsman, R., Sauer, F.D., Jackson, H.A., Wolynetz, M.S.: Methane and Carbon Dioxide Emissions
822 from Dairy Cows in Full Lactation Monitored over a Six-Month Period, *J. of Dairy Science*, 78
823 (12), 2760–2766, doi:10.3168/jds.S0022-0302(95)76907-7, 1995.

824 Kort, E. A., Frankenberg, C., Costigan, K. R., Lindenmaier, R., Dubey, M. K., and Wunch, D.: Four
825 corners: The largest US methane anomaly viewed from space, *Geophys. Res. Lett.*, 41, 6898–
826 6903, doi:10.1002/2014GL061503, 2014.

827 Lassen, J., Lovendahl, P., and Madsen, J.: Accuracy of noninvasive breath methane
828 measurements using Fourier transform infrared methods on individual cows, *J Dairy Sci.*, 95(2),
829 890–898, doi: 10.3168/jds.2011-4544, 2012.

830 Lauvaux, T., Schuh, A., Bocquet, M., Wu, L., Richardson, S., Miles, N., & Davis, K.: Network
831 design for mesoscale inversions of CO₂ sources and sinks. *Tellus B*, 64.
832 doi:10.3402/tellusb.v64i0.17980, 2012.

833 Lauvaux, T., and Davis, K. J. : Planetary boundary layer errors in mesoscale inversions of
834 column-integrated CO₂ measurements, *J. Geophys. Res. Atmos.*, 119, 490–508,
835 doi:10.1002/2013JD020175, 2014.

836 Lauvaux, T., Miles, N.L., Deng, A., Richardson, S. J., Cambaliza, M. O., Davis, K. J., Gaudet, B.,
837 Gurney, K. R., Huang, J., Karion, A., Oda, T., Patasaruk, R., Razlivanov, I., Sarmiento, D., Shepson,
838 P., Sweeney, C., Turnbull, J., and Wu, K.: High resolution atmospheric inversion of urban CO₂
839 emissions during the dormant season of the Indianapolis Flux Experiment (INFLUX), *J. Geophys.*
840 *Res. Atmos.*, 121, 5213–5236, doi:10.1002/2015JD024473, 2016.

841 Lavoie, T. N., Shepson, P. B., Cambaliza, M. O. L., Stirm, B. H., Karion, A., Sweeney, C., Yacovitch,
842 T. I., Herndon, S. C., Lan, X., and Lyon, D.: Aircraft-Based Measurements of Point Source
843 Methane Emissions in the Barnett Shale Basin, *Environ. Sci. Technol.*, 49 (13), 7904–7913, doi:
844 10.1021/acs.est.5b00410, 2015.

845 Leifer, I., Culling, D., Schneising, O., Farrell, P., Buchwitz, M., and Burrows, J. P.:
846 Transcontinental methane measurements: Part 2. Mobile surface investigation of fossil fuel
847 industrial fugitive emissions, *Atmos. Env.*, 74, 432–441,
848 <http://dx.doi.org/10.1016/j.atmosenv.2013.03.018>, 2013.

849 Lindenmaier, R., Dubey, M. K., Henderson, B. G., Butterfield, Z. T., Herman, J. R., Rahn, T., Lee,
850 S.-H.: Multiscale observations of CO₂, 13CO₂, and pollutants at Four Corners for emission
851 verification and attribution, *Proc. Natl. Acad. Sci. U. S. A.*, 111, 8386–8391, 2014.

852 McKain, K., Wofsy, S. C., Nehrkorn, T., Eluszkiewicz, J., Ehleringer, J. R., and Stephens, B. B.:
853 Assessment of ground-based atmospheric observations for verification of greenhouse gas
854 emissions from an urban region, *P. Natl. Acad. Sci. USA*, 109, 8423–8428,
855 doi:10.1073/pnas.1116645109, 2012.

856 Miller, S. M., Wofsy, S. C., Michalak, A. M., Kort, E. A., Andrews, A. E., Biraud, S. C., Dlugokencky,
857 E. J., Eluszkiewicz, J., Fischer, M. L., Janssens-Maenhout, G., Miller, B. R., Miller, J. B., Montzka,
858 S. A., Nehrkorn, T., and Sweeney, C.: Anthropogenic emissions of methane in the United States,
859 *P. Natl. Acad. Sci.*, 110 (50), 20018–20022, doi: 10.1073/pnas.1314391110, 2013.

860 Moeng, C.-H., Dudhia, J., Klemp, J., and Sullivan, P.: Examining two-way grid nesting for large
861 eddy simulation of the PBL using the WRF model, *Mon. Wea. Rev.*, 135, 2295–2311,
862 doi:10.1175/MWR3406.1, 2007.

863 Myhre, G., Shindell, D., Bréon, F.-M., Collins, W., Fuglestvedt, J., Huang, J., Koch, D., Lamarque,
864 J.-F., Lee, D., Mendoza, B., Nakajima, T., Robock, A., Stephens, G., Takemura, T., and Zhang, H.:
865 Anthropogenic and Natural Radiative Forcing. In: *Climate Change 2013: The Physical Science*
866 *Basis. Contribution of Working Group I to the Fifth Assessment Report of the Intergovernmental*
867 *Panel on Climate Change* [Stocker, T.F., Qin, D., Plattner, G.-K., Tignor, M., Allen, S.K., Boschung,
868 J., Nauels, A., Xia, Y., Bex, V. and Midgley, P.M. (eds.)]. Cambridge University Press, Cambridge,
869 United Kingdom and New York, NY, USA, 2013.

870 Nisbet, E., and Weiss, R.: Top-down versus bottom-up, *Science*, 328 (5983), 1241–1243,
871 doi:10.1126/science.1189936, 2010.

872 Nowak, J. B., Neuman, J. A., Bahreini, R., Middlebrook, A. M., Holloway, J. S. S., McKeen, S. A.,
873 Parrish, D. D. D., Ryerson, T. B. B., Trainer, M. K.: Ammonia sources in the California South Coast
874 Air Basin and their impact on ammonium nitrate formation, *Geophys. Res. Lett.*, 39, L07804,
875 doi:10.1029/2012GL051197, 2012.

876 Peischl, J., Ryerson, T. B., Brioude, J., Aikin, K. C., Andrews, A. E., Atlas, E., Blake, D., Daube,
877 B. C., de Gouw, J. A., Dlugokencky, E., Frost, G. J., Gentner, D. R., Gilman, J. B., Goldstein, A. H.,
878 Harley, R. A., Holloway, J. S., Kofler, J., Kuster, W. C., Lang, P. M., Novelli, P. C., Santoni, G. W.,
879 Trainer, M., Wofsy, S. C., and Parrish, D. D.: Quantifying sources of methane using light alkanes
880 in the Los Angeles basin, California, *J. Geophys. Res. Atmos.*, 118(10), 4974–4990,
881 doi:10.1002/jgrd.50413, 2013.

882 Rogers, R. E., Deng, A., Stauffer, D. R., Gaudet, B. J., Jia, Y., Soong, S., Tanrikulu, S.: Application
883 of the Weather Research and Forecasting Model for Air Quality Modeling in the San Francisco
884 Bay Area. *J. Appl. Meteor.*, 52, 1953-1973, 2013.

885 Skamarock, W. C., J. B. Klemp, J. Dudhia, D. O. Gill, D. M. Barker, M. G. Duda, X.-Y. Huang, W.
886 Wang, and J. G. Powers, 2008: A description of the Advanced Research WRF version 3. NCAR
887 Technical Note 475, http://www.mmm.ucar.edu/wrf/users/docs/arw_v3.pdf.

888 Streets, D.G., Canty, T., Carmichael, G.R., de Foy, B., Dickerson, R.R., Duncan, B.N., Edwards,
889 D.P., Haynes, J.A., Henze, D.K., Houyoux, M.R., Jacob, D.J., Krotkov, N.A., Lamsal, L.N., Liu, Y., Lu,

890 Z., Martin, R.V., Pfister, G.G., Pinder, R.W., Salawitch, R.J., Wecht, K.J.: Emissions estimation
891 from satellite retrievals: a review of current capability, *Atmos. Environ.*, 77, 1011–1042
892 <http://dx.doi.org/10.1016/j.atmosenv.2013.05.051>, 2013.

893 Stremme, W., Grutter, M., Rivera, C., Bezanilla, A., Garcia, A. R., Ortega, I., George, M.,
894 Clerbaux, C., Coheur, P.-F., Hurtmans, D., Hannigan, J. W., and Coffey, M. T.: Top-down
895 estimation of carbon monoxide emissions from the Mexico Megacity based on FTIR
896 measurements from ground and space, *Atmos. Chem. Phys.*, 13, 1357-1376, doi:10.5194/acp-
897 13-1357-2013, 2013.

898 Tilman, D. and Clark, M.: Global diets link environmental sustainability and human health,
899 *Nature*, 515, 518–522, doi:10.1038/nature13959, 2014.

900 Townsend-Small, A., Tyler, S.C., Pataki, D. E., Xu, X., and Christensen, L. E.: Isotopic
901 measurements of atmospheric methane in Los Angeles, California, USA reveal the influence of
902 “fugitive” fossil fuel emissions, *J. Geophysical Research*, 117, D7, doi:10.1029/2011JD016826,
903 2012.

904 US Climate Action Plan, strategy to reduce methane, full report,
905 [https://www.whitehouse.gov/sites/default/files/strategy_to_reduce_methane_emissions_201](https://www.whitehouse.gov/sites/default/files/strategy_to_reduce_methane_emissions_2014-03-28_final.pdf)
906 [4-03-28_final.pdf](https://www.whitehouse.gov/sites/default/files/strategy_to_reduce_methane_emissions_2014-03-28_final.pdf), March 2014.

907 Turner, A. J., Jacob, D. J., Wecht, K. J., Maasackers, J. D., Lundgren, E., Andrews, A. E., Biraud, S.
908 C., Boesch, H., Bowman, K. W., Deutscher, N. M., Dubey, M. K., Griffith, D. W. T., Hase, F., Kuze,
909 A., Notholt, J., Ohyama, H., Parker, R., Payne, V. H., Sussmann, R., Sweeney, C., Velazco, V. A.,
910 Warneke, T., Wennberg, P. O., and Wunch, D.: Estimating global and North American methane
911 emissions with high spatial resolution using GOSAT satellite data, *Atmos. Chem. Phys.*, 15,
912 7049-7069, doi:10.5194/acp-15-7049-2015, 2015.

913 Wennberg, P. O., Mui, W., Wunch, D., Kort, E. A., Blake, D. R. Atlas, E. L., Santoni, G. W., Wofsy,
914 S. C., Diskin, G. S., Joeng, S., and Fischer, M. L.: On the sources of methane to the Los Angeles
915 atmosphere, *Environ. Sci. Technol.*, 46 (17), 9282–9289, doi:10.1021/es301138y, 2012.

916 Wong, K. W., Fu, D., Pongetti, T. J., Newman, S., Kort, E. A., Duren, R., Hsu, Y.-K., Miller, C. E.,
917 Yung, Y. L., and Sander, S. P.: Mapping CH₄ : CO₂ ratios in Los Angeles with CLARS-FTS from
918 Mount Wilson, California, *Atmos. Chem. Phys.*, 15, 241-252, doi:10.5194/acp-15-241-2015,
919 2015.

920 Wunch, D., Wennberg, P. O., Toon, G. C., Keppel-Aleks, G., and Yavin, Y. G.: Emissions of
921 greenhouse gases from a North American megacity, *Geophys. Res. Lett.*, 36, L15810,
922 doi:10.1029/2009GL039825, 2009.

923 Wunch, D., Toon, G. C., Blavier, J.-F. L., Washenfelder, R. A., Notholt, J., Connor, B. J., Griffith, D.
924 W. T., Sherlock, V., and Wennberg, P. O.: The total carbon column observing network,
925 *Philosophical Transactions of the Royal Society - Series A: Mathematical, Physical and*
926 *Engineering Sciences*, 369(1943), 2087-2112, doi:10.1098/rsta.2010.0240, 2011.

927 Wunch, D., Toon, G. C., Sherlock, V., Deutscher, N. M., Liu, C., Feist, D. G. and Wennberg, P. O.:
928 The Total Carbon Column Observing Network's GGG2014 Data Version, 43,
929 doi:10.14291/tccon.ggg2014.documentation.R0/1221662, 2015.

930 York, D., Evensen, N. M., Lopez Martinez, M., and De Basabe Delgado, J.: Unified equations for
931 the slope, intercept, and standard errors of the best straight line, *Am J. Phys.*, 72(3), 367–375,
932 <http://dx.doi.org/10.1119/1.1632486>, 2004.

933 Zhao, C., Andrews, A. E., Bianco, L., Eluszkiewicz, J., Hirsch, A., MacDonald, C., Nehrkorn, T., and
934 Fischer, M. L.: Atmospheric inverse estimates of methane emissions from Central California, *J.*
935 *Geophys. Res.*, 114, D16302, doi:10.1029/2008JD011671, 2009.

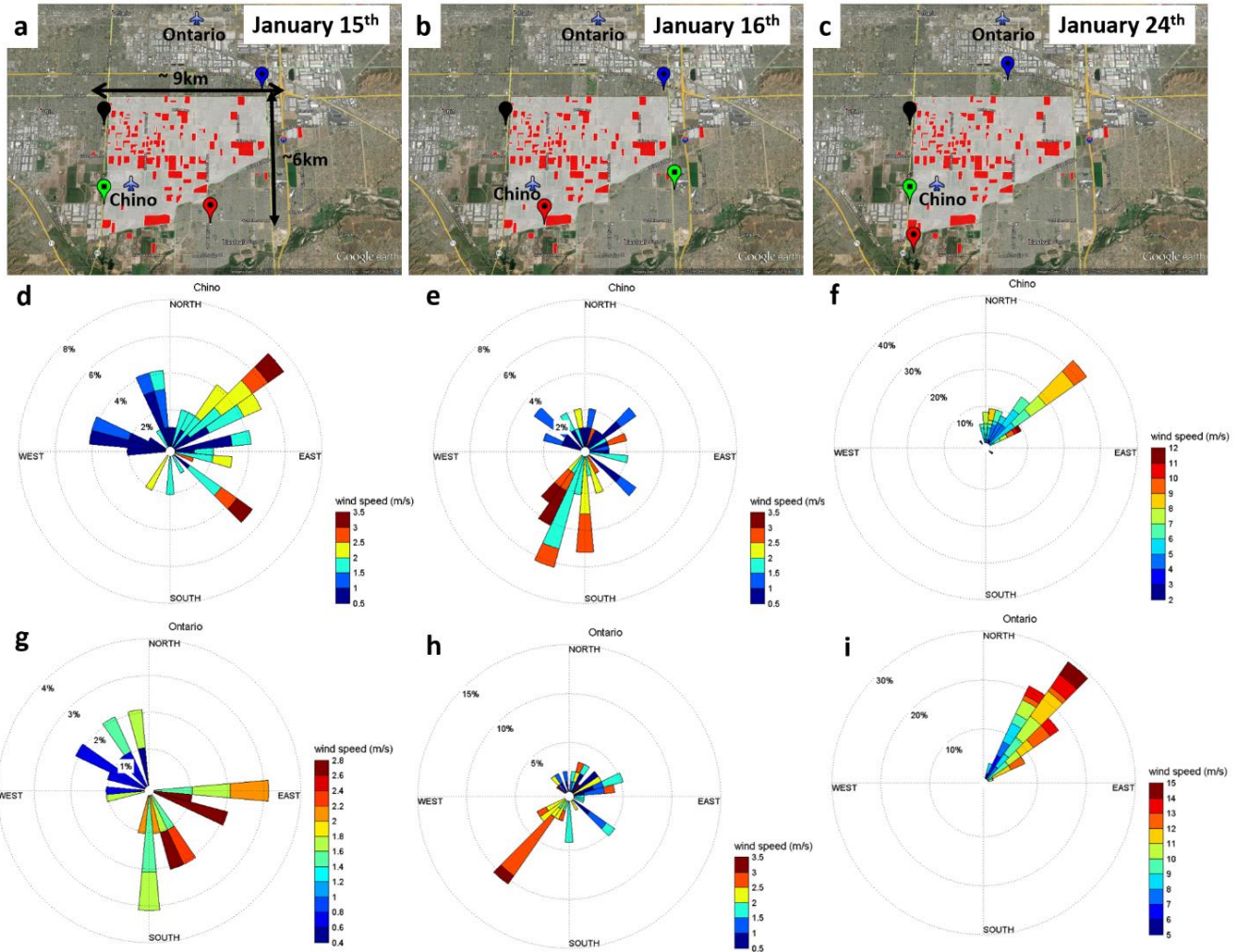
936

study	time of study	sources	CH ₄ emission (Gg/year)	CH ₄ emission (ppt/s)
Peischl et al., 2013	2010	inventory (dry manure + cows)	28	2.5
Peischl et al., 2013	2010	aircraft measurements	24-74	2.1-6.5
Wennberg et al., 2012	2010	inventory (wet manure + cows)*	66	5.8
CARB 2015	2015	inventory (dry manure + cows)	19	1.7
Chen et al., 2016	2015	FTS measurements only	19-32	1.7-3.3
This study	2015	FTS measurements only	16-55	1.4-4.8
This study	2015	WRF inversions	25-39	2.2-3.5

937

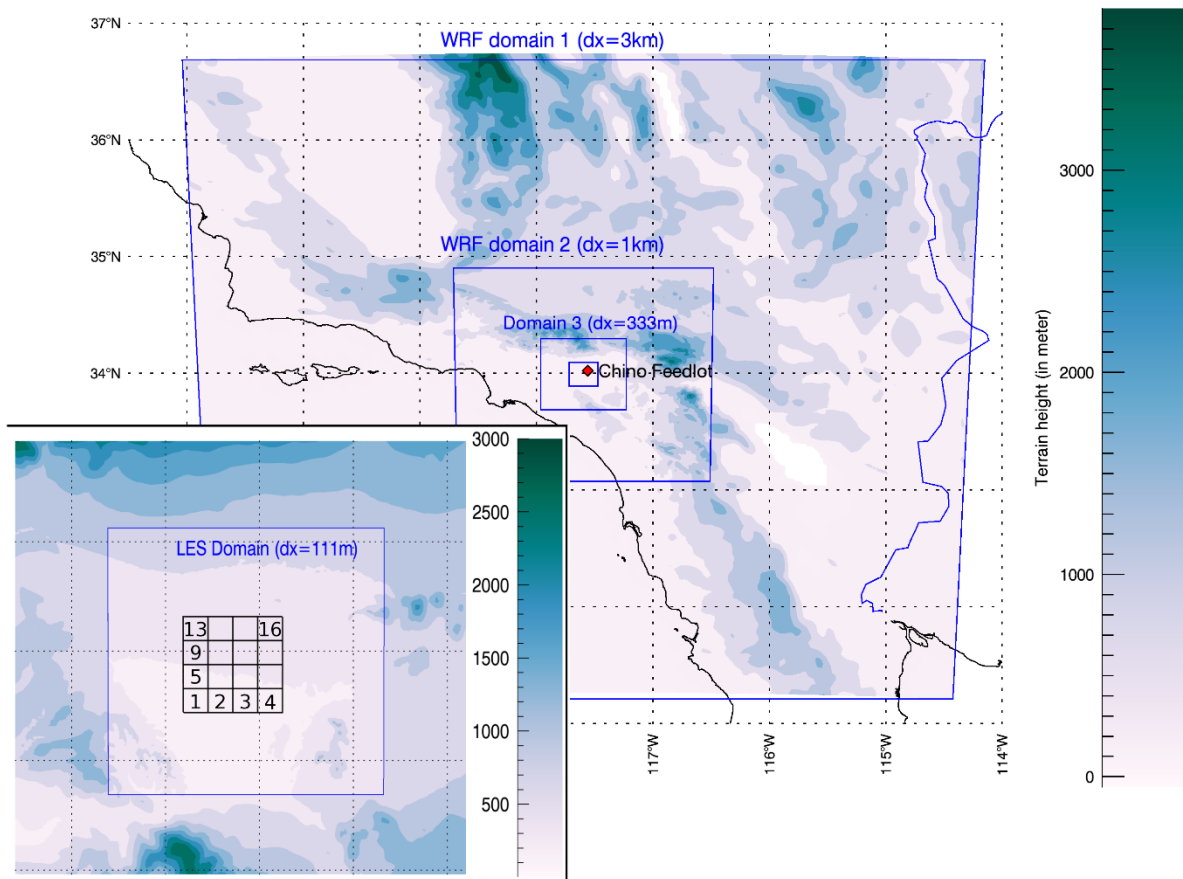
938 * Value reported for the SoCAB, apportioned for Chino in this study.

939 Table1: Emissions of CH₄ at Chino.



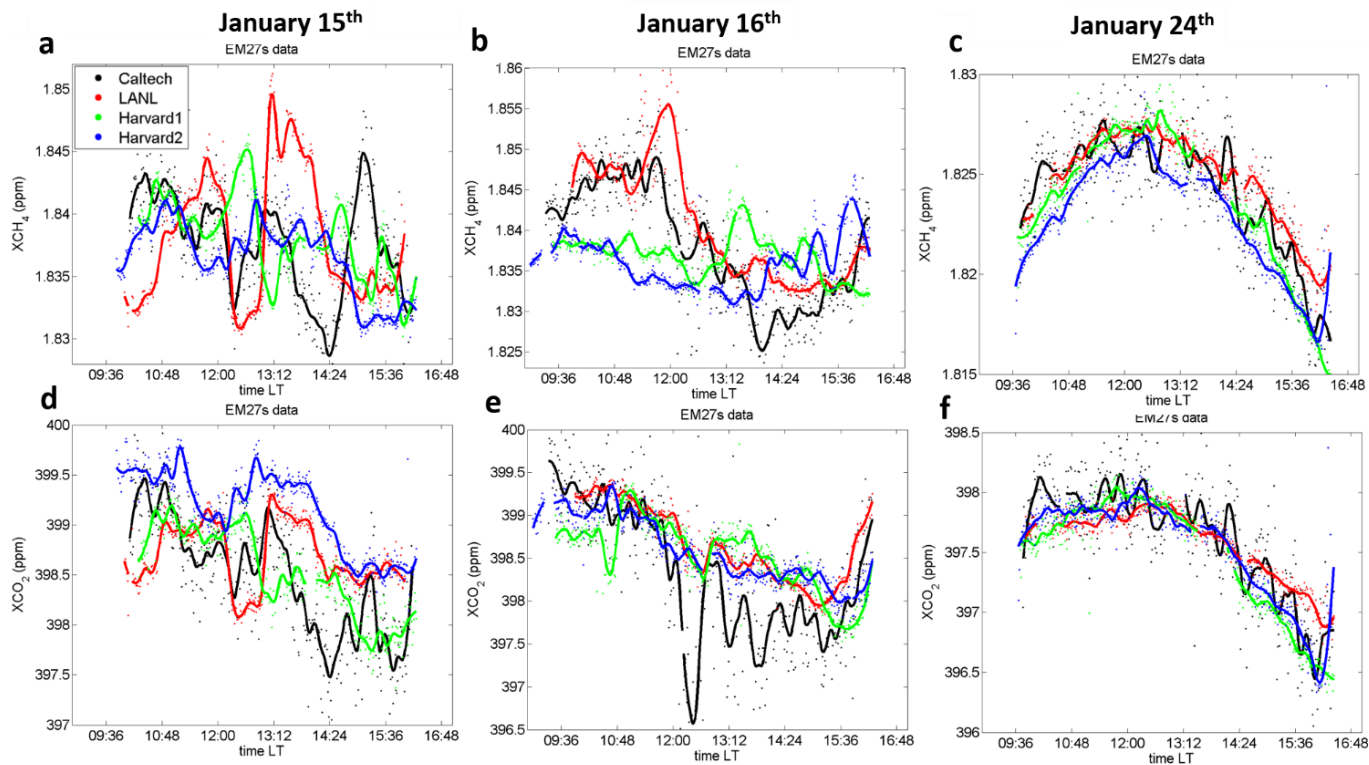
940

941 Figure 1: Three different days of measurements during the field campaign at Chino (~9 x 6 km) on the
 942 15th, 16th, and 24th of January 2015. Upper panels (a, b, and c) show the chosen locations of the four
 943 EM27/SUN (black, red, green, and blue pins correspond to the Caltech, LANL, Harvard1, and Harvard2
 944 instruments, respectively). The red marks on the map correspond to the dairy farms. Lower panels show
 945 wind roses of ten-minute average of wind directions and wind speeds measured at the two local airports
 946 (at Chino on panels d, e, and f, and at Ontario on panels g, h, and i). Map provided by GOOGLE EARTH V
 947 7.1.2.2041, US Dept. of State Geographer, Google, 2013, Image Landsat, Data SIO, NOAA, U.S. Navy,
 948 NGA, and GEBCO.



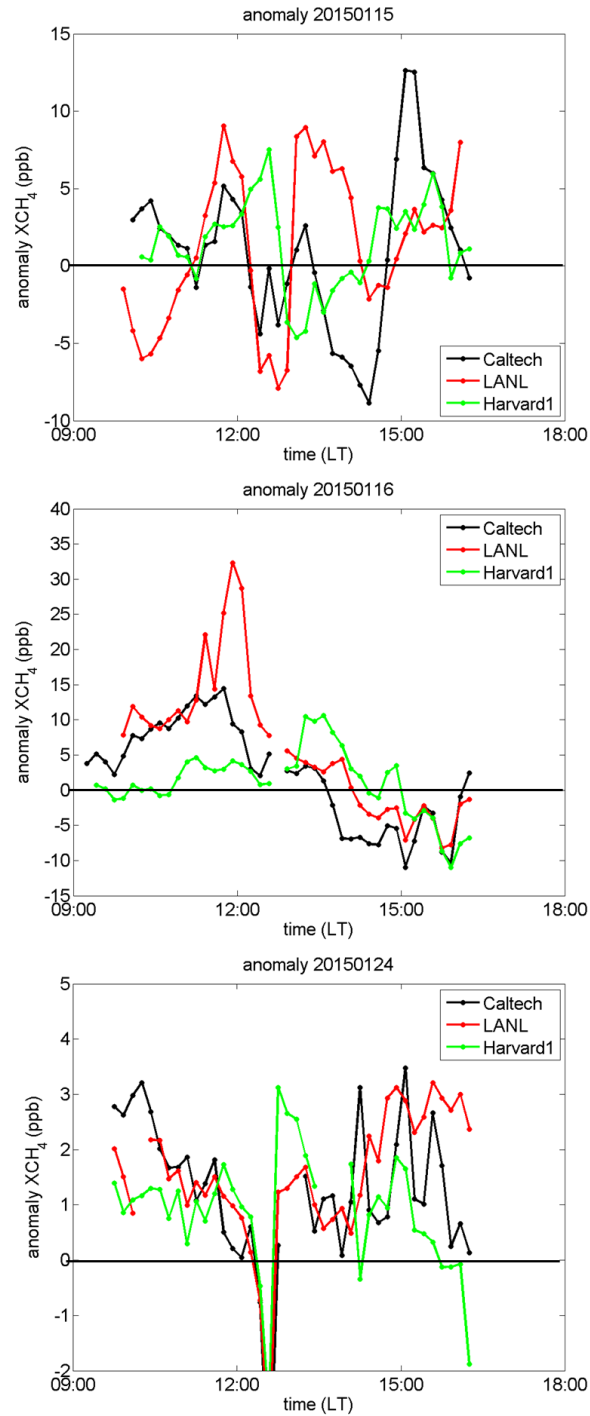
949

950 Figure 2: WRF-Chem simulation domains for the 4 grid resolutions (3-km; 1-km; 333-m; 111-m), with the
 951 corresponding topography based on the Shuttle Radar Topographic Mission Digital Elevation Model at
 952 90-m resolution). The 16 rectangular areas (2 x 2 km²) are shown on the LES domain map and numerate
 953 by pixel numbers (Figure 10).



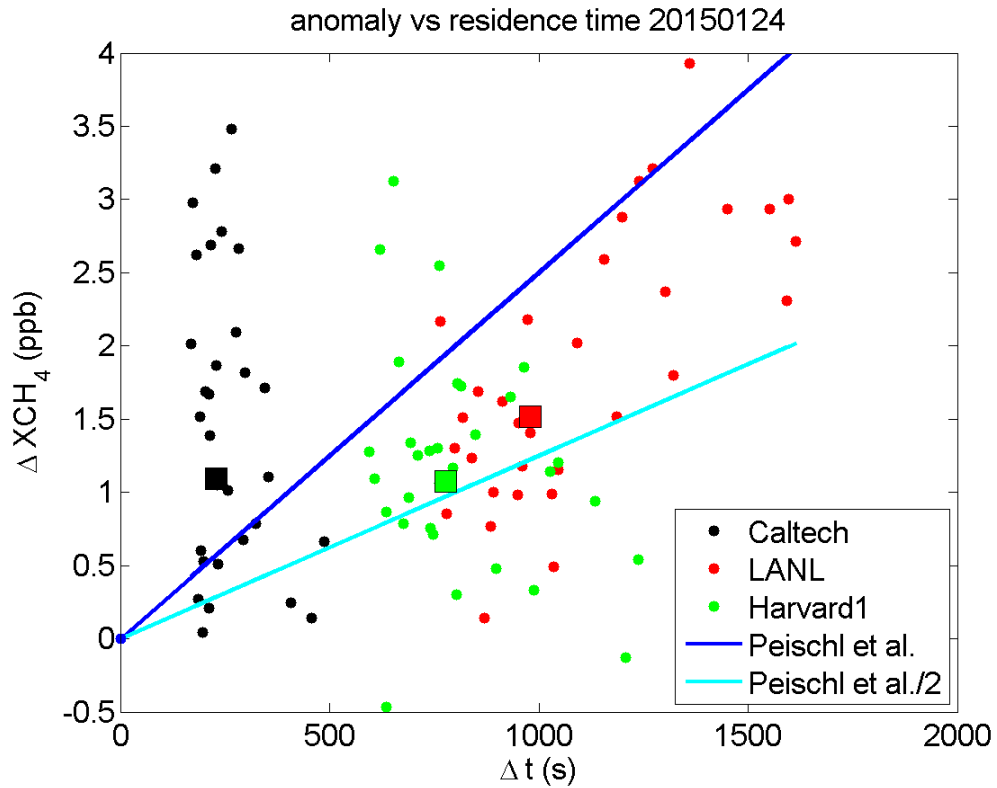
954

955 Figure 3: One minute-average time series of X_{CH_4} (upper panels a, b, and c)
 956 and f) measured by the four EM27/SUN (black, red, green, and blue marks correspond to the Caltech,
 957 LANL, Harvard1, and Harvard2 spectrometers, respectively).



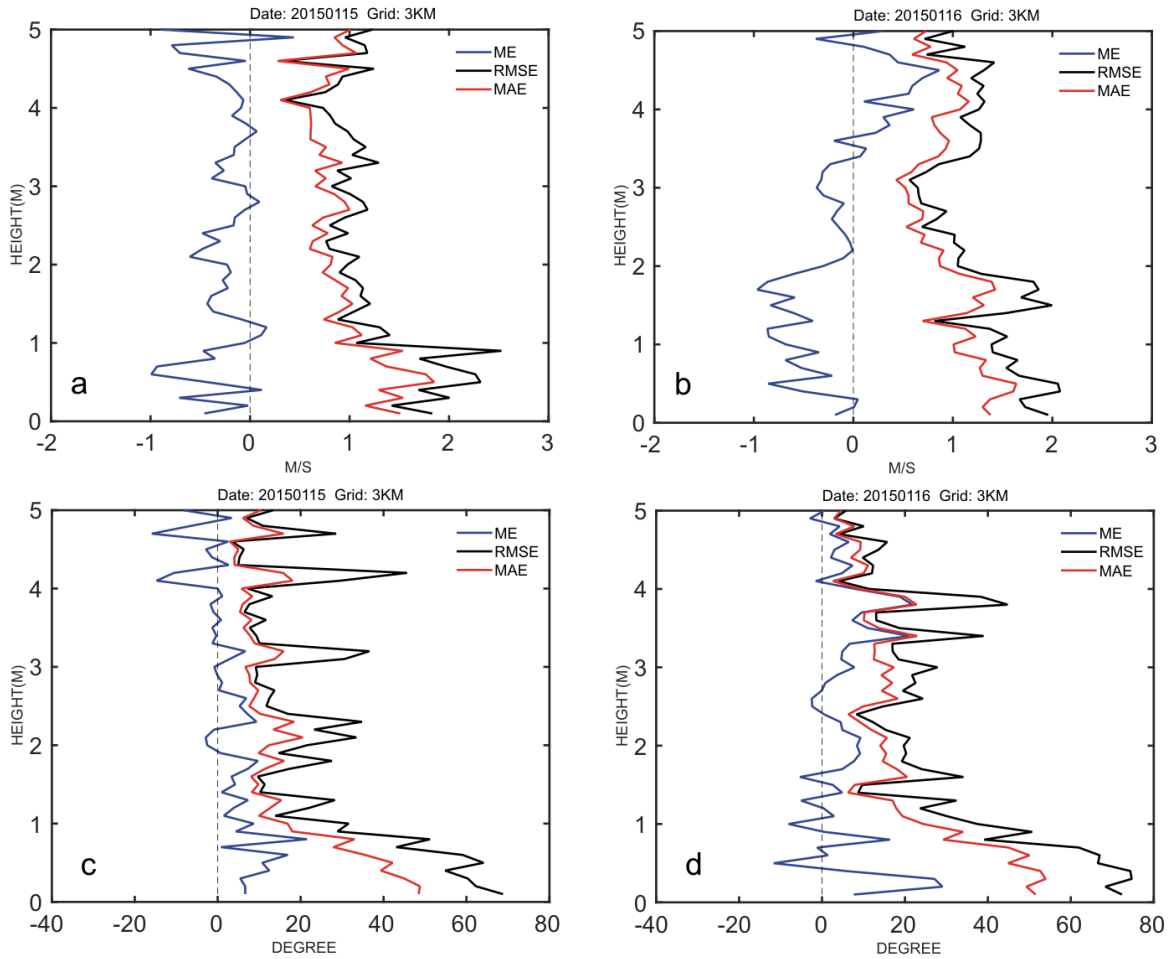
958

959 Figure 4: Time series of the 10-minute average X_{CH_4} anomaly ($\Delta_{X_{CH_4}}$, in ppb) computed relative to the
 960 Harvard2 instrument for January 15th (upper panel), January 16th (middle panel), and on January 24th
 961 2015 (lower panel).



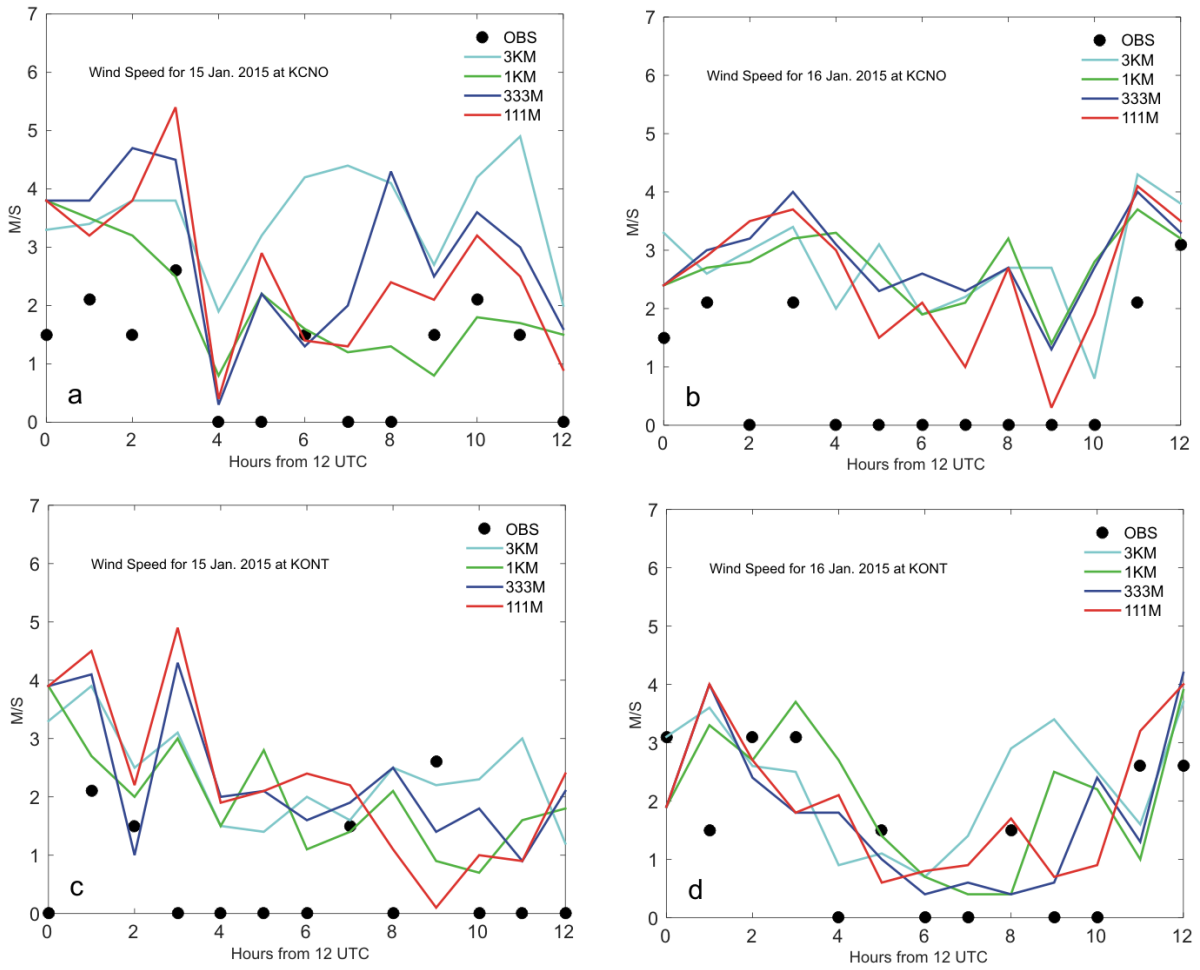
962

963 Figure 5: Estimated fluxes using FTS observations on January 24th. The 10-minute anomalies (relative to
 964 the Harvard 2 instrument) are plotted against the time that air mass travelled over the dairies, so that
 965 the slopes are equivalent to X_{CH_4} fluxes (in ppb/s, equation 5). The blue (and cyan) line represents the
 966 fluxes (and half of the value) estimated at Chino in 2010 (Peischl et al., 2013). The squares are the
 967 medians of the data which correspond to the estimated fluxes using the FTS observations (in black, red
 968 and green for the Caltech, LANL, and Harvard2 instruments).



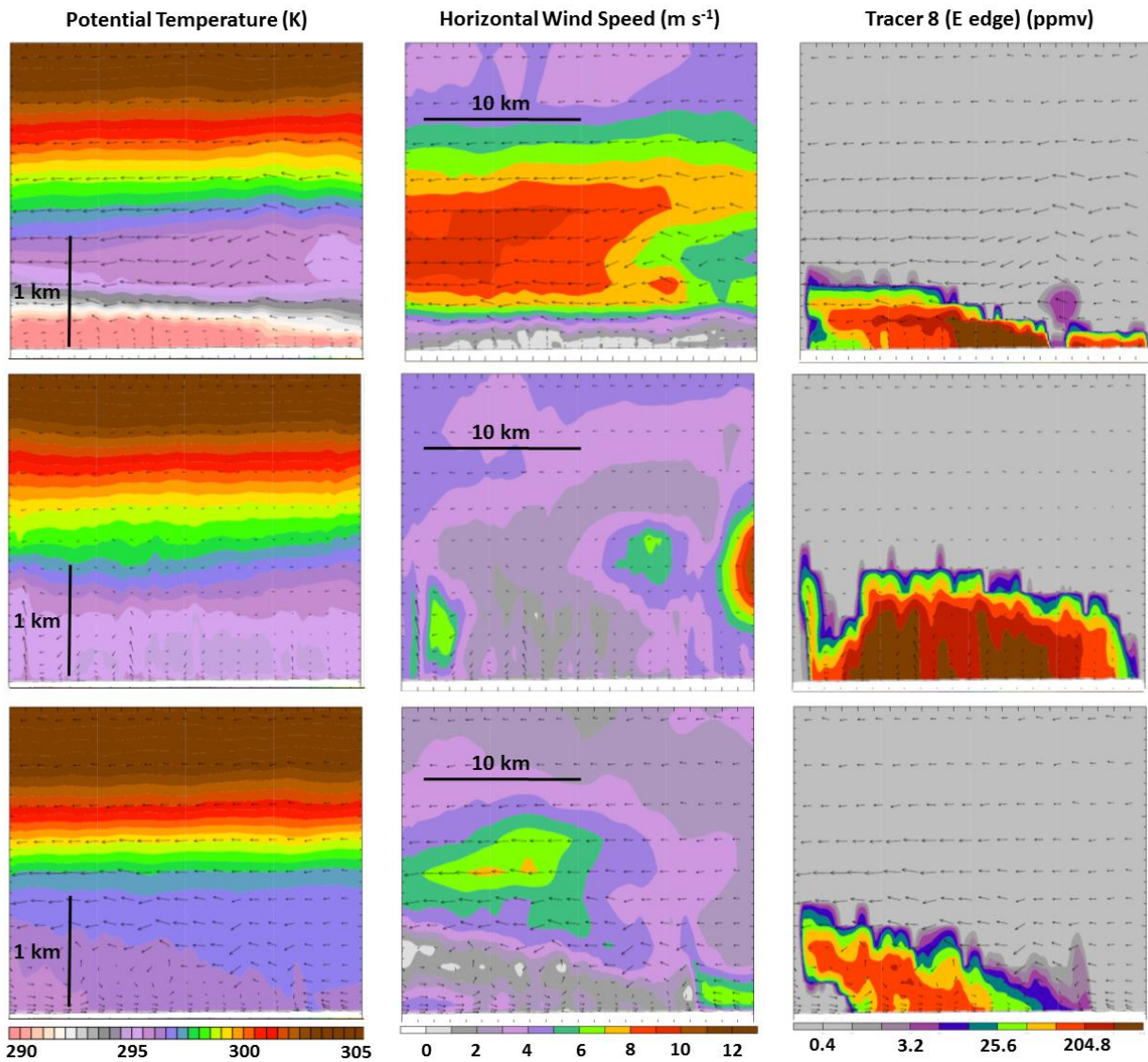
969

970 Figure 6: Vertical profiles of mean horizontal wind velocity errors (upper row) and direction (lower row)
 971 averaged from the WMO radiosonde sites available across the 3-km domain, with the Mean Absolute
 972 Error (in red), the Root Mean Square Error (in black), and the Mean Error (in blue). Only measurements
 973 from 00z radiosondes were used in the evaluation.



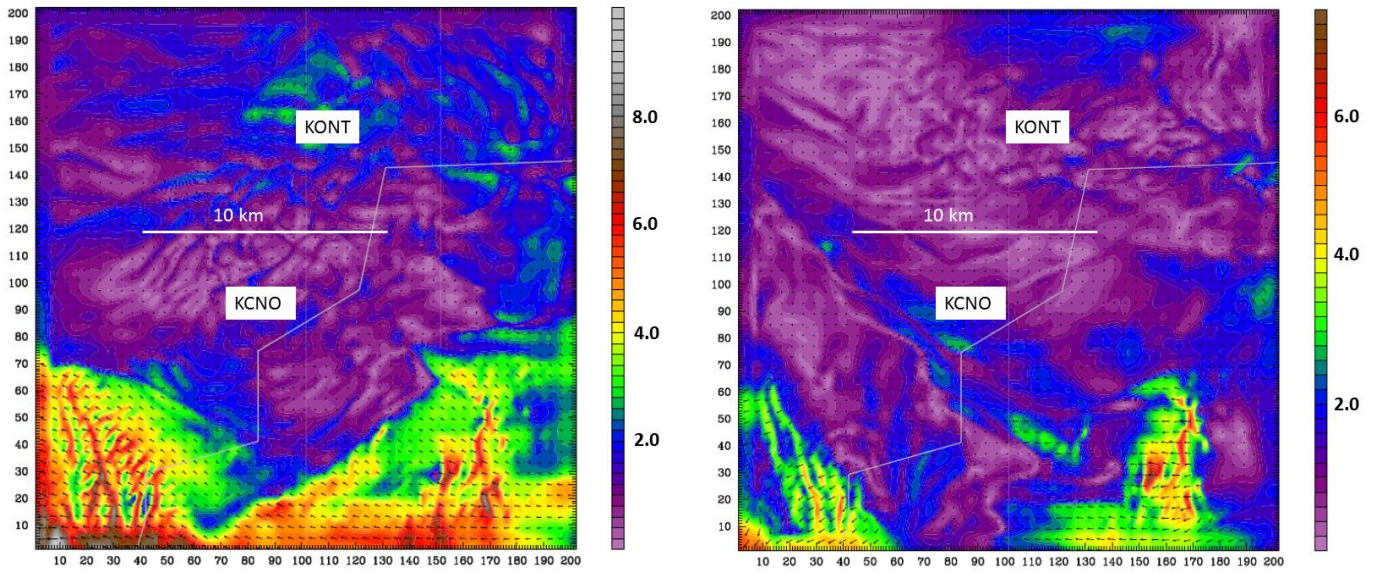
974

975 Figure 7: Mean horizontal 10-meter wind velocity in ms^{-1} measured at Chino (KCNO) and Ontario (KONT)
 976 airports for January 15th and 16th (black circles) compared to the simulated wind speed for different
 977 resolutions using WRF hourly-averaged results. When black circles indicate zero, the wind velocity
 978 measurements are below the WMO minimum threshold (i.e. 1.5 m/s).



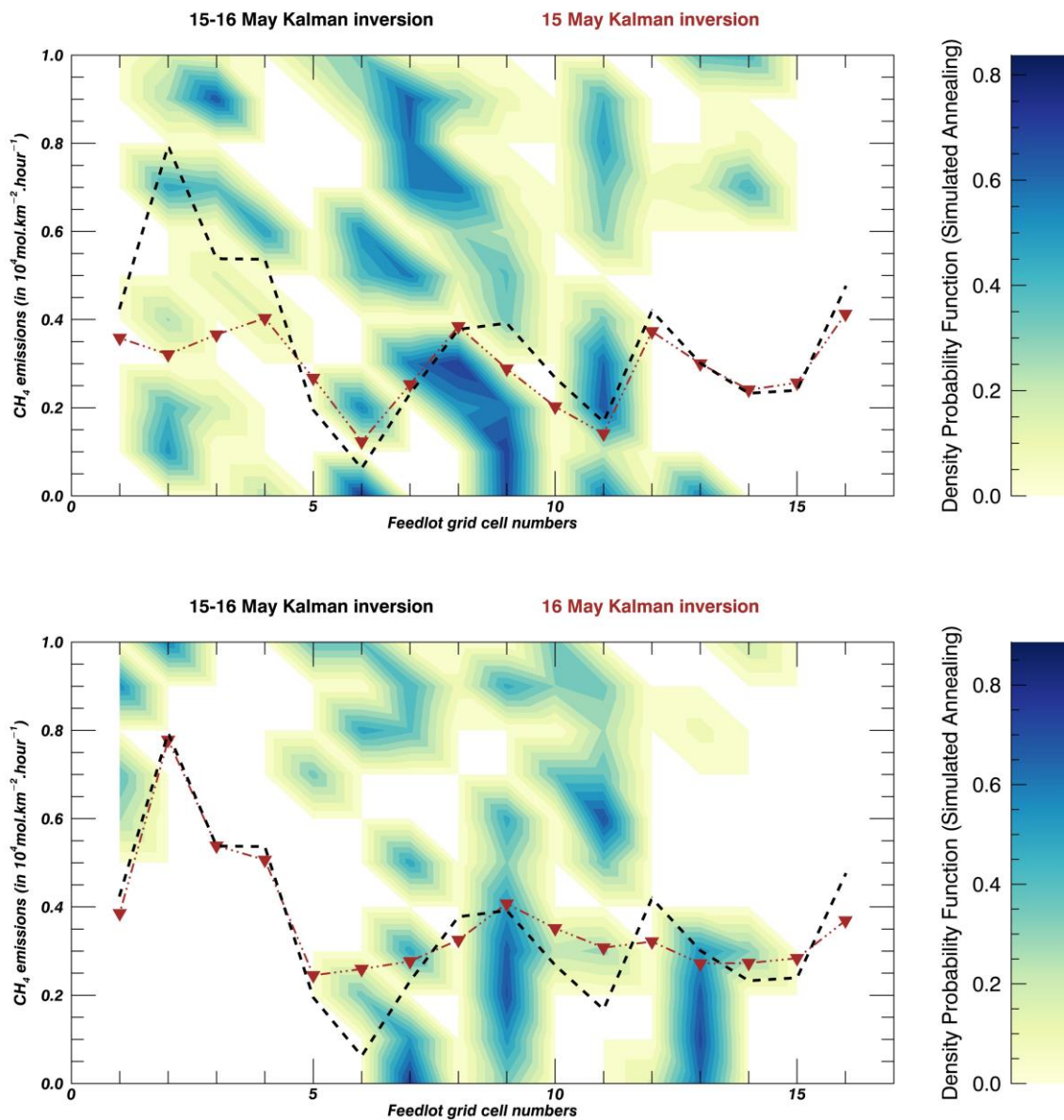
980

981 Figure 8: Vertical transects across the 111-m West-East WRF-LES simulation domain (pixels 5, 6, 7, and
 982 8) at 18:00 UTC of January 15th (upper row), 21:00 UTC (middle row), and 00:00 UTC (lower row). From
 983 left to right, simulated data are shown for potential temperature (in K, left column), mean horizontal
 984 wind speed and direction (in ms⁻¹ and degree, middle column), and passive tracer concentration
 985 released from an eastern pixel of the emitting area (pixel 5, right column), to illustrate the relationship
 986 between the three variables.



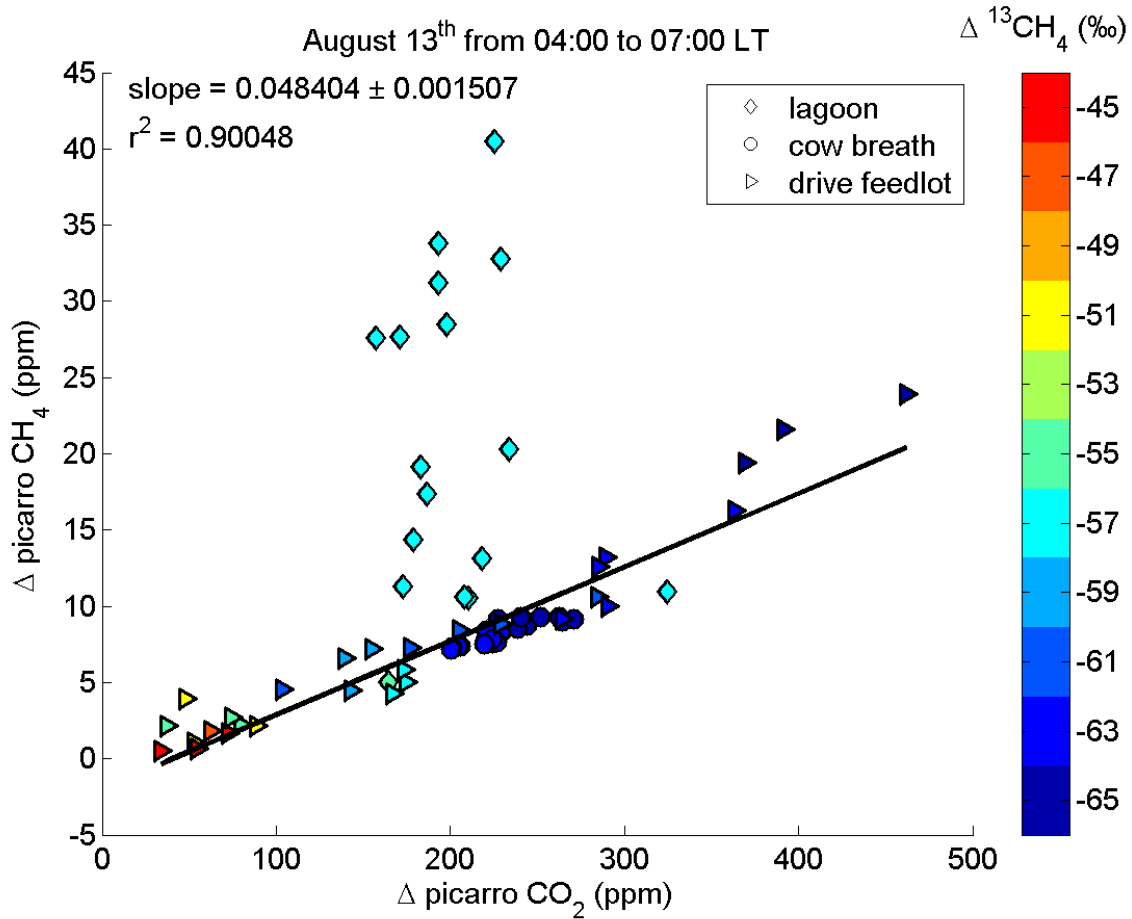
987

988 Figure 9: Mean horizontal wind field (in ms^{-1}) in the first level of the domain at 111-m resolution
 989 simulated by WRF-LES for January 15th (left panel), and January 16th 2015 (right panel), at 18:00 UTC.
 990 High wind speeds were simulated over the hills (southern part of the domain) whereas convective rolls,
 991 corresponding to organized turbulent eddies, are visible in the middle of the domain (i.e. over the
 992 feedlots of Chino), highlighting the importance of turbulent structures in representing the observed
 993 horizontal gradients of CH_4 concentrations. The locations of the Chino (KCNO) and Ontario (KONT)
 994 airports and the counties border (white line) are indicated.



995

996 Figure 10: Emissions of CH₄ (in mol/km²/hour) for the 16 pixels (2 x 2 km² shown In Figure 2) describing
 997 the dairies for both days, i.e. the 15th (upper panel) and 16th (lower panel) of January 2015. The
 998 Probability Density Function from the Simulated Annealing is shown in the background. The Bayesian
 999 mean emissions (see section 3.2) for the two days combined are shown in black (dash line) and for the
 1000 individual day (brown triangles).

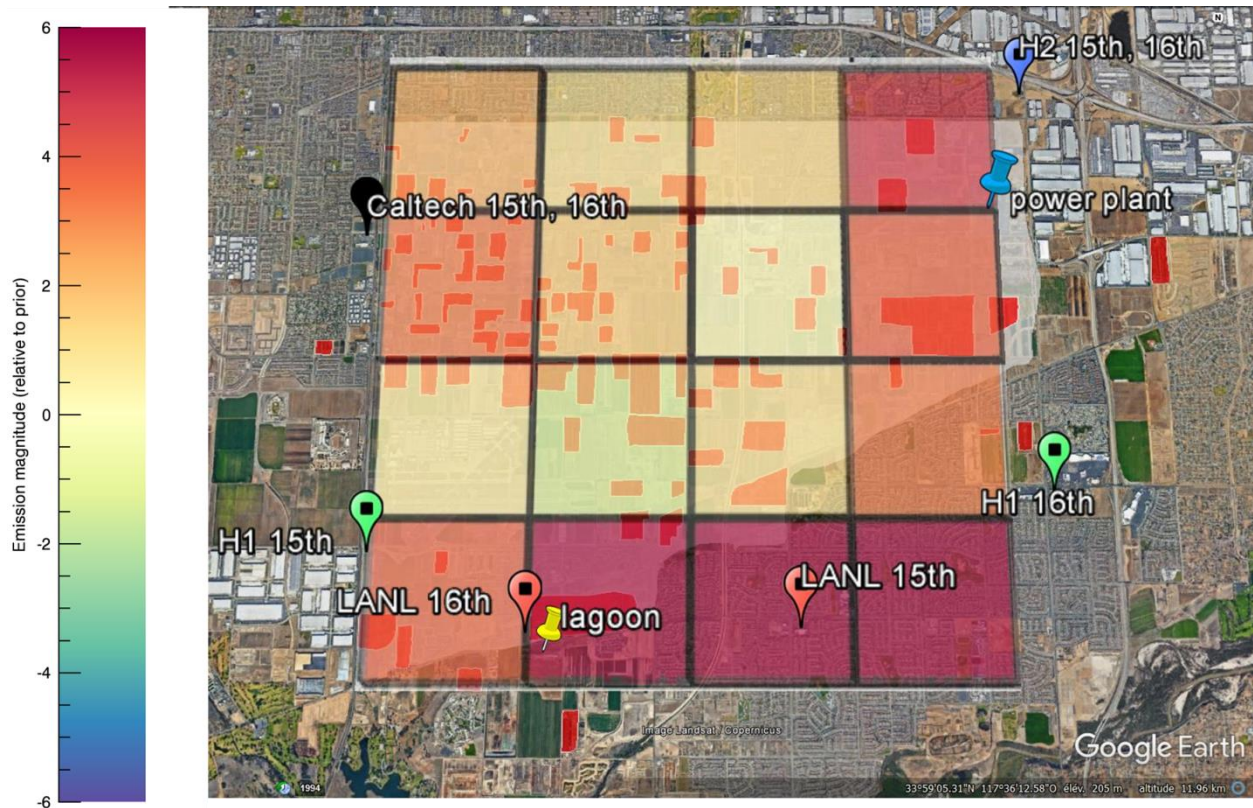


1001

1002 Figure 11: Scatter plot of one minute-average anomalies (from the 5 minutes smoothed) of CH_4 versus
 1003 CO_2 , color coded by the delta CH_4 values, measured by the Picarro on August 13th from 04:00 to 07:00
 1004 (LT).

1005

1006



1007
 1008 Figure 12: Map of the *a posteriori* X_{CH_4} fluxes (mean of January 15th and 16th runs) from the WRF-LES
 1009 simulations normalized by the *a priori* emissions and superimposed on a Google earth map, where the
 1010 dairy farms are represented by the red areas as shown in Figure 1. The domain is decomposed in 16
 1011 boxes (2km x 2km), in which the colors correspond to the *a posteriori* emissions from the WRF-LES
 1012 inversions. Red (blue) colors mean more (less) CH_4 emissions than dairy cows in that box. A
 1013 multiplicative ratio of 1 is equivalent to a flux of $2150 \text{ mol.km}^{-2}.\text{hour}^{-1}$. The locations of the lagoon
 1014 (yellow pin) and the power plant (blue pin) are also added on the map. Map provided by GOOGLE EARTH
 1015 V 7.1.2.2041, US Dept. of State Geographer, Google, 2013, Image Landsat, Data SIO, NOAA, U.S. Navy,
 1016 NGA, and GEBCO.